haematologica
Journal of the Ferrata Storti Foundation

ETV6::ACSL6 translocation-driven super-enhancer activation leads to eosinophilia in acute lymphoblastic leukemia through IL-3 overexpression

by Wenqian Xu, Feng Tian, Xiaolu Tai, Gaoxian Song, Yuanfang Liu, Liquan Fan, Xiangqin Weng, Eunjeong Yang, Meng Wang, Martin Bornhäuser, Chao Zhang, Richard B. Lock, Jason W.H. Wong, Jin Wang, Duohui Jing, and Jian-Qing Mi

Received: August 22, 2023.
Accepted: February 2, 2024.

Citation: Wenqian Xu, Feng Tian, Xiaolu Tai, Gaoxian Song, Yuanfang Liu, Liquan Fan, Xiangqin Weng, Eunjeong Yang, Meng Wang, Martin Bornhäuser, Chao Zhang, Richard B. Lock, Jason W.H. Wong, Jin Wang, Duohui Jing, and Jian-Qing Mi. ETV6::ACSL6 translocation-driven super-enhancer activation leads to eosinophilia in acute lymphoblastic leukemia through IL-3 overexpression. Haematologica. 2024 Feb 15. doi: 10.3324/haematol.2023.284121 [Epub ahead of print]

ETV6::ACSL6 translocation-driven super-enhancer activation leads to eosinophilia in acute lymphoblastic leukemia through IL-3 overexpression

Wenqian Xu[1]*, Feng Tian[2]*, Xiaolu Tai[3], Gaoxian Song[1], Yuanfang Liu[1], Liquan Fan[1], Xiangqin Weng[1], Eunjeong Yang[4], Meng Wang[5], Martin Bornhäuser[6], Chao Zhang[3], Richard B. Lock[7], Jason W.H. Wong[4], Jin Wang[1#], Duohui Jing[1#], Jian-Qing Mi[1#]

[1]Shanghai Institute of Hematology, State Key Laboratory of Medical Genomics, National Research Center for Translational Medicine at Shanghai, Ruijin Hospital Affiliated to Shanghai Jiao Tong University School of Medicine, Shanghai 200025, China

[2]Hebei Key Laboratory of Medical Data Science, Institute of Biomedical Informatics, School of Medicine, Hebei University of Engineering, Handan, Hebei Province, 056038, China

[3]Department of Plastic and Reconstructive Surgery, Shanghai Ninth People's Hospital, Shanghai Jiao Tong University School of Medicine, Shanghai, China

[4]School of Biomedical Sciences, University of Hong Kong, Hong Kong, China

[5]Songjiang Research Institute, Songjiang District Central Hospital, Institute of Autism & MOE-Shanghai Key Laboratory for Children's Environmental Health, Shanghai Jiao Tong University School of Medicine, Shanghai, China

[6]Medical Clinic I, University Hospital Carl Gustav Carus, TU Dresden, Dresden, Germany

[7]Children's Cancer Institute, Lowy Cancer Research Centre, School of Clinical Medicine, UNSW Medicine & Health, UNSW Centre for Childhood Cancer Research, UNSW Sydney, Sydney, NSW, Australia

* These authors contributed equally to this work.

\# These authors share senior authorship.

Corresponding authors

Duohui Jing, Shanghai Institute of Hematology, State Key Laboratory of Medical Genomics, National Research Center for Translational Medicine at Shanghai, Ruijin Hospital Affiliated to Shanghai Jiao Tong University School of Medicine, Shanghai 200025, China,

Tel: +8618217126794, Email: jdh12262@rjh.com.cn

Jin Wang, Shanghai Institute of Hematology, State Key Laboratory of Medical Genomics, National Research Center for Translational Medicine at Shanghai, Ruijin Hospital Affiliated to Shanghai Jiao Tong University School of Medicine, Shanghai 200025, China,

Tel: +8664370045-601803, Email: jinwang@shsmu.edu.cn
Jian-Qing Mi, Shanghai Institute of Hematology, State Key Laboratory of Medical Genomics, National Research Center for Translational Medicine at Shanghai, Ruijin Hospital Affiliated to Shanghai Jiao Tong University School of Medicine, Shanghai 200025, China,
Tel: +8664370045-601803, Email: jianqingmi@shsmu.edu.cn

Running title: Super-Enhancer Translocation in *ETV6::ACSL6* ALL

Total word count: 4000

Abstract word count: 199

Figures: 6

Table: 1

Funding

This research was funded by grants from the National Key R&D Program of China (2022YFE0200100), the Innovation Program of Shanghai Science and Technology Committee (23141903000, 21430711800), the National Natural Science Foundation of China (NSFC 82070144, 82270155, 82070227, 32271165, 82270187), the Mainland-Hong Kong Joint Funding Scheme supported by the Innovation and Technology Commission, the Government of Hong Kong SAR, China (MHP/054/21), the Ideas Grant funding of the National Health and Medical Research Council of Australia (APP1181666), and the Mobility Programme of the Joint Committee of the Sino-German Center for Research Promotion by the NSFC and the Deutsche Forschungsgemeinschaft (M-0337). RBL is supported by a fellowship from The National Health and Medical Research Council of Australia (NHMRC Fellowship APP1157871).

Acknowledgments

The authors thank Prof Heather Lee (University of Newcastle, Australia) for assistance in establishing the single-cell technique.

The authors acknowledge the ENCODE Consortium for generating DNaseI HS datasets and TF ChIP-seq datasets.

Author Contributions

DJ, JM and JW designed the study. WX performed experiments and analyzed the data.

FT performed bioinformatics analysis. WX, DJ and JM interpreted the data and wrote the manuscript. XT, GS and MW assisted in performing experiments. JM, JW, YL, LF and XW interpreted the clinical data. JWHW and E.Y. contributed to bioinformatics analysis. MB, CZ, RBL and JWHW contributed to the data interpretation and revision of the manuscript.

Competing interests

The authors declare no conflicts of interest. Any opinions, findings, conclusions or recommendations expressed in this publication do not reflect the views of The Government of the Hong Kong SAR, the Innovation and Technology Commission or the Vetting Committee of the Mainland-Hong Kong Joint Funding Scheme of the Innovation and Technology Fund.

Data Availability Statement

The raw sequencing data from this study have been deposited in the Genome Sequence Archive in National Genomics Data Center, Beijing Institute of Genomics (BIG), Chinses Academy of Sciences, under the accession number: HRA004277, that are publicly accessible at https://ngdc.cncb.ac.cn/gsa.

We also host a UCSC browser session for easy access and viewing of genome-wide mapping at:

http://genome-asia.ucsc.edu/s/xuwenqian/RJ9_data

All other relevant data that support the conclusions of the study are available from the authors on request. Please contact jdh12262@rjh.com.cn.

Keywords

Acute Lymphoblastic Leukemia, Eosinophilia, *ETV6* Fusion Gene, Super Enhancer Translocation, Chromatin Structural Variation

Abstract

ETV6::ACSL6 represents a rare genetic aberration in hematopoietic neoplasms and is often associated with severe eosinophilia, which confers an unfavorable prognosis requiring additional anti-inflammatory treatment. However, since the translocation is unlikely to produce a fusion protein, the mechanism of *ETV6::ACSL6* action remains unclear. Here, we performed multi-omics analyses of primary leukemia cells and patient-derived xenografts from an acute lymphoblastic leukemia (ALL) patient with *ETV6::ACSL6* translocation. We identified a super-enhancer located within the *ETV6* gene locus and revealed translocation and activation of the super-enhancer associated with the *ETV6::ACSL6* fusion. The translocated super-enhancer exhibited intense interactions with genomic regions adjacent to and distal from the breakpoint at chromosomes 5 and 12, including genes coding inflammatory factors such as *IL-3*. This led to modulations in DNA methylation, histone modifications, and chromatin structures, triggering transcription of inflammatory factors leading to eosinophilia. Furthermore, the bromodomain and extraterminal domain (BET) inhibitor synergized with standard-of-care drugs for ALL, effectively reducing *IL-3* expression and inhibiting *ETV6::ACSL6* ALL growth *in vitro* and *in vivo*. Overall, our study revealed for the first time a cis-regulatory mechanism of super-enhancer translocation in *ETV6::ACSL6* ALL, leading to ALL-accompanying clinical syndrome. These findings may stimulate novel treatment approaches for this challenging ALL subtype.

Introduction

Chromosomal rearrangements are common in cancers, particularly hematological malignancies(1). In acute lymphoblastic leukemia (ALL), their characterization has led to significant improvements in risk stratification and the development of targeted therapy(2, 3). *ETV6* is reported to form fusion genes with over 30 different partners, representing one of the most frequently translocated genes in ALL(4). While *ETV6::RUNX1*, a common *ETV6* fusion in children, indicates favorable outcomes(4), other *ETV6* fusions indicate poor prognosis(5, 6). In addition to standard-of-care chemotherapy, targeted therapies have been regularly applied in the clinic to inhibit the trans-regulatory activities of *ETV6* partner proteins(5, 7). Even though ETV6 is critical for hematopoiesis, its function in leukemogenesis may be underestimated compared to its partner proteins which play a dominant role in the dysregulation of downstream genes and pathways(7, 8). Moreover, the mechanisms, by which various *ETV6* fusions cause malignancy, remain poorly understood.

ETV6::ACSL6 t(5;12)(q31;p13) is a rare *ETV6* fusion, with only 17 cases reported in myeloid malignancies worldwide until 2022 and none in ALL. The prognosis of patients with *ETV6::ACSL6* is usually unfavorable, with most patients surviving less than a year(9). Eosinophilia is a common complication of the disease, which often results in damage to various organs. The elevated eosinophils, in severe cases, can cause cerebral infarction and heart failure, posing life-threatening risks. This complicates the clinical care of these patients and underscores the significance of prompt identification and treatment. Previous studies have found several pro-inflammatory mediators, including interleukin (IL)-3 and IL-5, to be upregulated in acute myeloid leukemia (AML) with *ETV6* t(5;12) translocations(10). While IL-5 is considered vital for the maturation and differentiation of eosinophils, IL-3 displays more potent effects on their functions(11). However, the mechanism of IL-3 and IL-5 upregulation in *ETV6::ACSL6* is yet to be elucidated.

Translocation events can induce trans- or cis-regulatory activities, altering gene expression profiles of cancer cells(12). Most previous studies focused on trans-regulatory activities of oncogenic fusion proteins(13-15). However, *ETV6::ACSL6* has been shown associated with frameshift mutation conferring a premature stop codon, thus unlikely to be translated into a full-length protein(16), suggesting an alternative mechanism involved. Cis-regulatory elements play critical roles in oncogenesis through structural variations (SVs). This may cause 'regulatory rearrangements' of promoters and enhancers, leading to dysregulation of oncogenes. For example, t(8;14)(q24;q32), the most common translocation in Burkitt lymphoma, leads to *MYC* overexpression due to the relocation of an enhancer from chromosome (chr) 14 to its nearby region(17). Further, in 2004, it was shown that the ectopic expression of the homeobox gene *CDX2* resulting from the t(12;13)(p13;q12) and not the expression of the *ETV6::CDX2* fusion gene resulted in AML in a murine model(18). Recently, *ETV6* was also demonstrated to regulate its partner gene *MN1* via super-enhancer (SE) hijacking in AML(19). However, the mechanism is yet to be extended to other *ETV6* fusions as well as genes apart from its partners, and the clinical relevance of *ETV6*-associated SE hijacking events remains unexplored.

Coding genes of inflammatory factors, including *IL-3*, *IL-5* and *GM-CSF*, are located adjacent to *ACSL6* on chr5. This raises a question of whether and how *ETV6::ACSL6* is involved in the dysregulation of these genes. Therefore, in this study, we performed multi-omics approach to interrogate the *ETV6* translocation-induced cis-regulatory mutation and changes in the 3D genome structure in *ETV6::ACSL6* ALL, thus, to decipher mechanisms of inflammatory factor dysregulation and its associated clinical syndrome eosinophilia.

Methods

Bone marrow samples from patients

Bone marrow samples from ALL patients or the healthy donor (diagnosed with thrombocytopenia, but both bone marrow smear and flow cytometry showing no abnormalities) were obtained under informed consent from Ruijin Hospital. Mononuclear cells were enriched by density gradient centrifugation with Ficoll solution. The use of samples was approved by the institution review board. All relevant ethical regulations were followed in this study.

scNMT-seq library preparation and sequencing

scNMT-seq libraries were prepared according to a previous protocol(20). Single cells were sorted using FACS Aria into 96-well plates containing 2.5μl of reaction buffer

(1×M.CviPI buffer (NEB), 2 U M.CviPI (NEB), 160 μM S-adenosylmethionine (NEB), 1 U μl−1 RNasein (Thermo), 0.1% IGEPAL CA-630 (Sigma)). After a 15-minute incubation at 37 °C, add RLT plus buffer (Qiagen) and store samples at −80 °C. Poly-A RNA was captured on oligo-dT and amplified cDNA was prepared according to Smart-seq2 protocols. The gDNA lysate was purified on AMPureXP beads before bisulfite-sequencing (BS-seq) libraries were prepared according to the scBS-seq protocol(21). Sequencing was carried out on a NovaSeq instrument, with a mean raw sequencing depth of 7.5 million (BS-seq) and 5 million (RNA-seq) paired-end reads per cell. BS-seq alignment and methylation/accessibility quantification was performed following a previous approach(20). Briefly, each cell's individual CpG or GpC sites were modeled using a binomial distribution, where the number of successes represented the reads supporting methylation, and the number of trials was the total read count. The CpG methylation or GpC accessibility rate for each site and cell was determined through maximum likelihood estimation. Subsequently, the rates were rounded to the nearest integer (0 or 1).

All other methods are described in detail in Supplementary data.

Results

Transcriptomic analysis of *ETV6::ACSL6* ALL and its accompanied eosinophils

The *ETV6::ACSL6* ALL patient is a 66-year-old male presenting to the clinic with dry cough. The eosinophil count has consistently been greater than 1.5×10^9/L for over five years. The patient demonstrated elevated eosinophils (black arrow) in the peripheral blood and bone marrow (Fig. 1A). Two distinct populations of ALL cells and eosinophils were observed by flowcytometry analysis, with ALL cells exhibiting classic immunophenotype ($CD19^+CD45^{dim}CD10^+CD20^-CD38^{dim}CD58^+$) (Fig. 1B). Monitoring blood routine of the patient, we found similar dynamics of cell counts in ALL and eosinophils following induction therapy (Supplementary Fig. S1). The karyotype revealed 46,XY,t(5;12)(q31;p13),del(11)(p15)[1]/46,XY[23]. RNA-seq was performed on the two populations individually after flow-sorting and *ETV6::ACSL6* was only detected in lymphoblast, while eosinophils did not carry this fusion gene. This indicates that the eosinophil expansion seems to be reactive rather than a clonal proliferation caused by genetic aberrations. Furthermore, analyzing gene expression profiles (GEP) from RNA-seq datasets, we found that *IL-3* and *IL-5* were highly expressed in ALL and eosinophils compared to the normal bone marrow sample (Fig. 1C). The result was confirmed by RT-qPCR (Fig. 1D). This indicates an intrinsic correlation between inflammatory factors produced by ALL and its accompanied eosinophils with normal karyotype.

Next, comparing GEPs of the *ETV6::ACSL6* ALL with previously published RNA-seq datasets of ALL(22, 23), we found that the *ETV6::ACSL6* ALL was clustered with eosinophils, mono-nuclear cells from a healthy bone marrow, and GM12878 cells, but distinct from a well-studied *ETV6* translocation, *ETV6::RUNX1* fusion, suggesting a distinct mechanism of *ETV6::ACSL6* in promoting malignancy transformation (Fig. 1E). We further analyzed the top 10 genes that were differentially expressed (also enriched on chr5 and chr12) in the *ETV6::ACSL6* ALL and other ALL subtypes. Interestingly, genes adjacent to the breakpoint of chr5 were significantly upregulated, including *P4HA2*, *SLC22A5*, *ACSL6*, *IL-3* and *IL-5* (13 Kb, 300 Kb, 40 Kb, 7 Kb and 480 Kb from the breakpoint respectively), while genes distant from *ETV6* on chr12, such as *PRH1* and *APOLD1* (480 Kb and 1.1 Mb from the breakpoint respectively), were down-regulated (Fig. 1F). This indicates that the perturbations in the ALL transcriptome not only resulted from the potential intragenic SE of *ETV6* promoting genes on chr5, but also from the inactivation of genes on chr12 with the deprivation of *ETV6* regulation.

Multi-omics analysis of *IL-3* activation in *ETV6::ACSL6* ALL

To further delineate genetic basis of the fusion gene, we performed long-read sequencing on ALL cells using Oxford Nanopore Technologies (ONT). Both RNA-seq (Fig. 2A) and ONT-seq (Fig. 2B) demonstrated a breakpoint at the first intron of *ETV6*. RNA-seq identified a fusion of the 1st exon of *ETV6* with the 2nd exon of *ACSL6* in mRNA (Fig. 2A, C), however, instead of a DNA break at the *ACSL6* locus, the ONT data revealed a breakpoint at the intergenic region of *ACSL6* and *IL-3* on chr5 (Fig. 2B). These data indicate that the fusion of *ETV6* to *ACSL6* revealed by RNA-seq may be due to alternative splicing which skipped the 1st exon of *ACSL6*，as shown in the schematics in Fig. 2D. We also detected genetic aberrations at various genomic regions, functions of which are yet to be defined (Fig. 2E, Supplementary Table S1, Supplementary Table S2, Supplementary Fig. S2).

The two derivative chromosomes in *ETV6::ACSL6* ALL, i.e. an *ETV6::ACSL6* (EA) strand and an *IL3::ETV6* (IE) strand, are illustrated in Supplementary Fig. S3 and verified by RT-PCR in Supplementary Fig. S4A. Analyzing RNA-seq data, we identified a frameshift mutation leading to a premature stop codon (Supplementary Fig. S4B). To confirm the result, we ectopically expressed a full-length EA transcript in Nalm6 (pre-B ALL) cells with a flag peptide at the end of *ACSL6* (Supplementary Fig S4C). As a control, a wild-type *ETV6*-Flag vector was also transduced, which demonstrated an Over-Expression of ETV6 and flag proteins (ETV6-OE, Supplementary Fig. S4C). However, while expression of the EA transcript was verified by PCR (Supplementary Fig. S4D), neither size shift of the ETV6 protein nor the expression of flag was detected (Supplementary Fig. S4E). In summary, *ETV6::ACSL6* does not give rise to a fusion protein, consistent with previous reports(6).

Given the scarcity of patient samples, we performed single cell multi-omics sequencing (scNMT-seq) on ALL cells and eosinophils (Supplementary Fig. S5A). UMAP reduction of scRNA data revealed two clusters: a majority ALL cluster expressing cancer-associated genes like *ZFP36L2*, *SF3B1*, and *ARHGDIB*(24-26), and a smaller cluster comprising eosinophils and some ALL cells (Fig. 2F, Supplementary Fig. S5B). Gene set enrichment analysis (GSEA) revealed differentially expressed genes between ALLs and eosinophils enriched in hypoxia, unfolded protein response, and DNA repair (p53) pathways, which are reported frequently activated in tumors(27) (Fig. 2G). Performing scNMT-seq in different subtypes showed that the *IL-3* promoter (orange shading) revealed less enriched methylated-CpG and higher enriched methylated-GpC (accessibility) in the *ETV6::ACSL6* ALL (RJ-9) compared to another ALL (RJ-10) with a normal karyotype (Fig. 2H, Supplementary Fig. S5C). The dot plots demonstrated CpG and GpC methylation status in each cells indicating a highly activated *IL-3* in *ETV6::ACSL6* ALL single cells. Moreover, eosinophils exhibited less GpC methylation (accessibility) and higher CpG methylation at the *IL-3* locus than the *ETV6::ACSL6* ALL cells (Supplementary Fig. S5D). Taken together, our data suggest that the *ETV6* translocation altered epigenetic features at genomic regions beyond its fusion partner at chr5.

Furthermore, we extracted enrichments of methylated-CpG and -GpC at promoters for individual cells. Integrating DNA methylation (mCpG), accessibility (GpCm), and RNA transcription through multi-omics factor analysis (MOFA) revealed three clusters (Supplementary Fig. S5E), highlighting the epigenetic heterogeneity. mRNA contributed less to cluster identification compared to DNA methylation and chromatin accessibility (5%, 41% and 46% variance in top 5 MOFA factors; Supplementary Fig. S5F). We then profiled the top 50 differentially methylated regions, identifying two leukemia cells with higher chromatin accessibility and hypomethylation in genes such as *TCF12*, *LIN52* (Supplementary Fig. S5G) that were reported to promote tumor progression(28, 29). Enrichment analysis revealed involvement of metabolic and energetic pathways (Supplementary Fig. S5H), suggesting a connection between metabolic perturbance with epigenetic changes in *ETV6::ACSL6* ALL.

Overall, our data suggest that the *ETV6* translocation induced critical epigenetic changes at the gene locus adjacent to the breakpoint on the two derivative chromosomes, however, mechanisms causing the abnormal epigenetics remains to be identified.

Chromatin structural variation induced by *ETV6* super-enhancer translocation

Next, we performed SE analysis to explore enhancer activities in diverse cell types. Extracting cell-type specific SEs from the SEdb database, encompassing lymphoid, myeloid and other non-hematopoietic cell types, we observed distinctive blood-specific SEs, notably the *ETV6* locus (Fig. 3A). This suggests that ETV6 serves not only as a crucial transcription factor but also as an indispensable intragenic hematopoiesis-specific SE in both lymphoid and myeloid cells. In order to validate our findings in *ETV6::ACSL6* ALL, we analyzed H3K4me1 (primed and active enhancers), H3K27ac (activated enhancers), BRD4 and p300 enrichments at the *ETV6* locus (Fig. 3B). Prominent enrichments of H3K27ac and H3K4me1 were identified at the *ETV6* locus, with BRD4, the reader of H3K27ac, was also present in this region. The enriched H3K27ac was also observed in B-ALL with normal karyotype (ALL-50 from our previous studies(22)) and cell lines from ENCODE database(30), suggesting the *ETV6* intragenic region functions as an SE in cis-regulatory machinery. Using the ROSE algorithm(31), the 200 Kb (chr12:11718965-11902194) region was recognized as a highly-confident SE (Fig. 3C). Interestingly, compared to Nalm6, an ALL cell line with *ETV6::PDGFR* fusion, REH with *ETV6::RUNX1* showed decreased H3K27ac enrichment at the *ETV6* locus (Fig. 3D), indicating a diminished SE activity in REH. Therefore, the activity of the intragenic SE seems to be various in different *ETV6* fusions.

The *ETV6* locus was split into two sections: Pro-SE1(green rectangle) including the *ETV6* promoter plus a minor SE at the left side; SE2 (blue rectangle) representing the major SE at the right side (Fig. 3E). To verify the enhancer activities of two sections, we selected a 3Kb region (orange shading) from each section based on transcription factor (TF) binding density and chromatin accessibility (DNase I Hypersensitive Site, DHS) from the ENCODE database and inserted them into a luciferase reporter vector (Fig. 3F). As shown in Fig. 3G, while both Pro-SE1- and SE2-inserted vectors revealed significantly enhanced luminescence compared to control, the SE2-inserted vector demonstrated a much prominent luminescence signal indicating a heritage of the SE activity. Motif analysis revealed potential binding sites for TFs related to lymphocyte-development/malignancy at the SE, such as Smad3, PAX5 and others (Fig. 3H). Overall, the two sections of the *ETV6* locus derived from the translocation event maintain enhancer activities, indicating their potential role in regulating ALL genes.

SEs are clusters of enhancers tightly interacting with multiple adjacent or distal genes(32). Using high-throughput chromosome conformation capture (Hi-C), we investigated mechanisms of *ETV6*-SE interacting with target genes on a genome-wide scale. *ETV6::ACSL6* ALL displayed a butterfly morphology at the intersection of chr5 and chr12 in the Hi-C heatmap (dotted circles in Fig. 4A), whereas GM12878 showed blank, confirming translocation only in RJ-9. Next, using a web-based genome browser(33), we observed strong interactions between Pro-SE1 and *ACSL6*, enhancing *ACSL6* transcription and H3K27Ac modification in RJ-9 (green dashed lines, Fig. 4B). SE2 interacted with multiple downstream genes of *ACSL6*, including strong interactions with *IL-3*, *P4HA2* and a slight interaction with *IL-5* (blue dashed lines, Fig. 4B). Consistent with their normally silent state in lymphocytes, GM12878 displayed no active signals for these genes (Fig. 4C). Hi-C contact intensities revealed the formation of new topologically associated domains (TADs) spanning the breakpoints with CTCF binding at boundaries, which constrained regulatory activities of Pro-SE1 and SE2, and restricted their target genes (Fig. 4D). Neoloop finder identified 69 interchromosomal neoloops were found on IE and 7 on EA(34), suggesting uneven activities of Pro-SE1 and SE2 in regulating genes (Supplementary Fig. S6). To validate the regulatory effects of the newly formed TADs, we compared gene expression profiles within and outside of the TADs. *ETV6::ACSL6* ALL revealed an upregulation of genes located within the TADs compared to GM12878, whereas genes outside of the TADs did not exhibit significant expression perturbations (Fig. 4E). Furthermore, the sustained activity of *ETV6* was also observed in the patient sample with *ETV6::RUNX1*, where the translocated *ETV6* exhibited strong interactions with its partner, *RUNX1*(35). In *ETV6::ACSL6* ALL, among all genes that are activated due to enhancer hijacking, IL-3 and IL-5 are supposed to promote eosinophilia in patients, besides, P4HA2, a proline hydrolase, has been shown to be associated with poor prognosis of diffuse large B-cell lymphoma(36). Studying *P4HA2* expression in our previously reported ALL patients(37) by RNA-seq and qPCR, we found that patients with high expression of *P4HA2* had lower survival rates (Supplementary Fig. S7), indicating that *P4HA2* dysregulation by SE2 may contribute to the poor prognosis of these patients. Overall, our data suggest that hijacking the two sections derived from *ETV6*-SE altered three-dimensional genomic organization at new locations, triggering gene transcription exclusively in the *ETV6::ACSL6* ALL and led to its unique clinical characteristics.

BETi partially reversed gene dysregulation in *ETV6::ACSL6* ALL

The biological function of SE is often mediated by bromodomain proteins like BRD4 that recognizes highly-enriched acetylated histones at the SEs. The bromodomain inhibitor JQ1 has been shown to disrupt enhancer functions, with more pronounced effect on SEs(38). Performing *in vitro* treatment of JQ1 on a patient-derived xenograft (PDX) of the *ETV6::ACSL6* ALL, 1163 genes were significantly upregulated and 1925 downregulated, including a decrease in *IL-3* (Fold change: 0.535887, $p < 0.001$) and a mild decrease in *IL-5* (Fig. 5A, B). Notably, *MYC* and *BCL2* were also downregulated in agreement with previous reports on JQ1-induced gene regulation(39). GSEA revealed inhibited cytokine and Myc-targets pathways (Fig. 5C). RT-qPCR confirmed that exposing cells to JQ1 decreased *IL-3* expression in a time- and concentration-dependent manner (Fig. 5D). Consistent with this observation, IL-3 concentration in the medium of *ETV6::ACSL6* PDX cell culture decreased after JQ1 treatment, in contrast, *ETV6::RUNX1* cells showed no IL-3 in the medium before and after JQ1 treatment (Fig. 5E). As a control, Jurkat cells were pre-stimulated by phytohemagglutinin and phorbol myristate acetate to activate *IL3* expression and followed with JQ1 treatment for 12 hours. RT-qPCR showed a decrease of 50% in *IL3* mRNA after JQ1 treatment, which was significantly lower than the *IL3* decrease in the *ETV6::ACSL6* ALL (Supplementary Fig. S8). Since the *IL3* expression in Jurkat cells without an SE translocation is supposed to be regulated by a regular enhancer at *IL3* upstream(40), this suggests a stronger dependency on BRD4 by SEs. Moreover, BRD4 binding was substantially reduced at the whole-genome level and the *ETV6* locus upon JQ1 treatment (Fig. 5F-H). Consistent with previous reports(39), JQ1 altered the genome-wide BRD4 distribution, decreasing at promoters and increasing at intergenic regions (Fig. 5I). Therefore, JQ1 holds promise for dampening gene dysregulation in *ETV6::ACSL6* ALL.

Cytotoxicity of BETi treatment on *ETV6::ACSL6* ALL *in vitro* and *in vivo*

We then assessed JQ1's cytotoxic effects on *ETV6::ACSL6* ALL *in vitro* and *in vivo*. Treatment with JQ1 at concentrations >100nM significantly reduced cell viability *in vitro*, with limited effect on other genetic lesions (Fig. 6A, Supplementary Table S3). JQ1 was then tested in combination with standard-of-care drugs against the *ETV6::ACSL6* ALL. Our data demonstrated synergistic effects of JQ1 with vincristine and doxorubicin, and an additive effect with dexamethasone *in vitro*, with ZIP scores of 24.9, 25.0 and 6.88 respectively (Fig. 6B and Supplementary Fig. S9A). Notably, while vincristine or doxorubicin alone achieved 50-70% inhibition of cell viability, the addition of JQ1 (1μM) substantially decreased the IC_{50} and reduced cell viability to around 10% (Fig. 6C and Supplementary Fig. S9B). Furthermore, we tested five other commonly-used BET inhibitors: ABBV-744, Birabresib, I-BET151, Mivebresib and PFI-1, and observed their synergistic cytotoxicity with vincristine in treating *ETV6::ACSL6* ALL (Table 1, Supplementary Fig. S9C). Next, *in vivo* treatments were performed as shown in Fig. 6D. RT-qPCR revealed a significant decrease in *IL-3* expression following 24-hour *in vivo* treatment of JQ1 and vincristine (Fig. 6E). The combination treatment significantly inhibited tumor growth in spleen, bone marrow and peripheral blood at day 28, compared to single-drug treatment with vincristine or JQ1 (Fig. 6F, Supplementary Fig. S10A, B). Additionally, we observed that the spleens of the mice in the combination group were dramatically reduced in size after 28 days of treatment compared to those treated with vincristine alone (Supplementary Fig. S10C). One-week post-treatment, the mice treated with vincristine experienced relapse, while the combination group maintained remission for another 7 days (Fig. 6G). Survival analysis also showed that the combination treatment significantly prolonged the median event-free survival of mice by 9.2 days compared to vincristine alone (Fig. 6H). Overall, our data suggest that combining first-line chemotherapy with JQ1 is promising to improve the treatment of *ETV6::ACSL6* B-ALL patients.

Discussion

Chromosome translocations often lead to fusion oncogenes, generating fusion proteins interfering with signaling transduction in cancer cells. However, our study confirmed that SVs can impact tumor behavior by altering gene expression through enhancer hijacking(34). In *ETV6::ACSL6* leukemia, a frameshift-induced stop codon prevents protein formation, rendering the fusion protein theory insufficient for explaining eosinophilia. Furthermore, the eosinophils did not carry *ETV6::ACSL6*, indicating eosinophilia as a paraneoplastic syndrome. Our study identified an SE at the *ETV6* locus and revealed that in *ETV6::ACSL6* ALL, the *ETV6*-SE was split into two parts, both exhibiting enhancer activities. This altered chromatin organization in derivative chromosomes, which enhanced the expression of IL-3 and other inflammatory factors, leading to eosinophilia in patients. Our study provides novel insights into cis-regulatory mutation mechanisms associated with this ALL subtype and its clinical complication.

In several *ETV6*-translocation subtypes, fusion proteins were reported to play a dominant role in oncogenesis, most of which function as transcription factors or kinases(41). For instance, *ETV6::RUNX1*, constituting 13% of B-ALL, was reported to mediate oncogenic activity as a transcription factor(14). However, mechanisms beyond the trans-regulation by fusion proteins have been poorly studied. In 2021, *ETV6* was reported for the first time to contain an intragenic SE triggering expression of its partner gene *MN1* in *ETV6::MN1* AML(19). In our study, while Hi-C may not be the optimal technique for quantifying enhancer hijacking events, limiting our ability to accurately assess the interactions between regions, it is still useful for detecting new interactions from the translocated SE and target genes. The translocated

ETV6 regulated not only its fusion partner *ACSL6*, but also distant genes such as *IL-3*, leading to a critical clinical syndrome (eosinophilia) in ALL. Our future work will extend our findings to other *ETV6* fusion partners to gain a comprehensive understanding of the cis-regulatory mechanisms in *ETV6* ALL subtypes.

Our data highlight cis-regulatory mutations controlling the expression of multiple genes, offering potential targets for precision therapy. IL-3, studied for over 30 years, induces proliferation of various cell types, including eosinophils and malignant hematopoietic cells like AML(42). IL-3 and GM-CSF are crucial in MYC-transduced human hematopoietic cells transitioning to AML, suggesting a crucial role of cytokines in tumorigenesis(43). Furthermore, *ACSL6* and a distal gene *P4HA2* were also activated by the SE translocation. ACSL6, a long-chain acyl-CoA synthetase, catalyzes long-chain fatty acids(44). Even though the function of ACSL6 in leukemia is not fully understood, its expression was shown to correlate with the prognosis of AML(45). Our preliminary studies indicated *P4HA2*'s association with ALL prognosis, which aligns with previous findings in diffuse large B-cell lymphoma(36). However, the oncogenic role of SE-induced gene overexpression in *ETV6::ACSL6* ALL remains unclear, which will be addressed in further studies. Nevertheless, according to the "multi-hit" theory in oncogenesis(46), SE-induced gene dysregulation may cooperate with other genetic variations driving leukemia transformation and progression.

Eosinophilia accompanying hematological malignancies has diverse causes, including neoplastic, reactive, or idiopathic. The WHO 2022 classification includes "Myeloid/Lymphoid neoplasms with eosinophilia" (M/LN-Eo) as a separate category, with gene rearrangements of *PDGFRA*, *PDGFRB* and others(47). In M/LN-Eo with clonal eosinophilia, gene rearrangements can be detected in eosinophils and other myeloid/lymphoid cell lineages, suggesting pluripotential hematopoietic progenitor cell origin. Conversely, reactive eosinophilia often results from tumors secreting cytokines, such as IL-3. Examples of such tumors include Hodgkin lymphoma(48) and our case *ETV6::ACSL6* ALL. Therefore, it is critical to determine different treatment strategies, considering varied causal mechanisms of eosinophilia in hematological malignancies.

Besides glucocorticoids, the conventional treatment for eosinophilia, other targeted options are being explored. Clonal eosinophilia bearing fusion genes may benefit from TKIs(47), but limited choices exist for reactive eosinophilia, which often causes severe symptoms and hinders primary disease treatment. In *ETV6::ACSL6* ALL, with eosinophilia linked to elevated IL-3, drugs targeting IL-3 pathways are considered. Furthermore, BRD4 inhibitors have achieved promising anti-tumor effects in various preclinical studies(49). Since the translocated SE conferring IL-3 elevation was highly enriched with BRD4, its inhibition significantly dampened the SE-induced gene expression, and synergize with first-line chemo-drugs in treating *ETV6::ACSL6* ALL *in vitro* and *in vivo*. This demonstrates the potential of new therapeutic approaches for *ETV6::ACSL6* ALL.

Overall, our study reports for the first time that *ETV6* translocation led to chromatin structural variations in ALL patients, which resulted in dysregulation of inflammatory factors conferring eosinophilia in ALL. This highlighted the crucial role of enhancer hijacking in oncogenesis and particularly its clinical complications, and provided insights into improving treatment strategies for this ALL subtype with unfavorable prognosis.

References

1. Mitelman F, Johansson B, Mertens F. The impact of translocations and gene fusions on cancer causation. Nat Rev Cancer. 2007; 7(4):233-245.

2. Li JF, Dai YT, Lilljebjörn H, et al. Transcriptional landscape of B cell precursor acute lymphoblastic leukemia based on an international study of 1,223 cases. Proc Natl Acad Sci U S A. 2018;115(50):E11711-E11720.

3. Chen B, Jiang L, Zhong ML, et al. Identification of fusion genes and characterization of transcriptome features in T-cell acute lymphoblastic leukemia. Proc Natl Acad Sci U S A. 2018;115(2):373-378.

4. Rasighaemi P, Ward AC. ETV6 and ETV7: Siblings in hematopoiesis and its disruption in disease. Crit Rev Oncol Hematol. 2017;116(2):106-115.

5. Zaliova M, Moorman AV, Cazzaniga G, et al. Characterization of leukemias with ETV6-ABL1 fusion. Haematologica. 2016;101(9):1082-1093.

6. Zhou MH, Gao L, Jing Y, et al. Detection of ETV6 gene rearrangements in adult acute lymphoblastic leukemia. Ann Hematol. 2012;91(8):1235-1243.

7. Bain BJ, Ahmad S. Should myeloid and lymphoid neoplasms with PCM1-JAK2 and other rearrangements of JAK2 be recognized as specific entities? Br J Haematol. 2014;166(6):809-817.

8. Zimmermannova O, Doktorova E, Stuchly J, et al. An activating mutation of GNB1 is associated with resistance to tyrosine kinase inhibitors in ETV6-ABL1-positive leukemia. Oncogene. 2017;36(43):5985-5994.

9. Su Z, Liu X, Hu W, et al. Myeloid neoplasm with ETV6::ACSl6 fusion: landscape of molecular and clinical features. Hematology. 2022;27(1):1010-1018.

10. Cools J, Mentens N, Odero MD, et al Evidence for position effects as a variant ETV6-mediated leukemogenic mechanism in myeloid leukemias with a t(4;12)(q11-q12;p13) or t(5;12)(q31;p13). Blood. 2002;99(5):1776-1784.

11. Esnault S, Kelly EA. Essential Mechanisms of Differential Activation of Eosinophils by IL-3 Compared to GM-CSF and IL-5. Crit Rev Immunol. 2016;36(5):429-444.

12. Patel B, Kang Y, Cui K, et al. Aberrant TAL1 activation is mediated by an interchromosomal interaction in human T-cell acute lymphoblastic leukemia. Leukemia. 2014;28(2):349-361.

13. Huang Y, Mouttet B, Warnatz HJ, et al. The Leukemogenic TCF3-HLF Complex Rewires Enhancers Driving Cellular Identity and Self-Renewal Conferring EP300 Vulnerability. Cancer Cell. 2019;36(6):630-644.

14. Polak R, Bierings MB, van der Leije CS, et al. Autophagy inhibition as a potential future targeted therapy for ETV6-RUNX1-driven B-cell precursor acute lymphoblastic leukemia. Haematologica. 2019;104(4):738-748.

15. Adnan-Awad S, Kim D, Hohtari H, et al. Characterization of p190-Bcr-Abl chronic myeloid leukemia reveals specific signaling pathways and therapeutic targets. Leukemia. 2021;35(7):1964-1975.

16. Yagasaki F, Jinnai I, Yoshida S, et al. Fusion of TEL/ETV6 to a novel ACS2 in myelodysplastic syndrome and acute myelogenous leukemia with t(5;12)(q31;p13). Genes Chromosomes Cancer. 1999;26(3):192-202.

17. López C, Burkhardt B, Chan JKC, et al. Burkitt lymphoma. Nat Rev Dis Primers. 2022;8(1):78.

18. Rawat VP, Cusan M, Deshpande A, et al. Ectopic expression of the homeobox gene Cdx2 is the

transforming event in a mouse model of t(12;13)(p13;q12) acute myeloid leukemia. Proc Natl Acad Sci U S A. 2004;101(3):817-822.

19. Riedel SS, Lu C, Xie HM, et al. Intrinsically disordered Meningioma-1 stabilizes the BAF complex to cause AML. Mol Cell. 2021;81(11):2332-2348.

20. Argelaguet R, Clark SJ, Mohammed H, et al. Multi-omics profiling of mouse gastrulation at single-cell resolution. Nature. 2019;576(7787):487-491.

21. Clark SJ, Smallwood SA, Lee HJ, Krueger F, Reik W, Kelsey G. Genome-wide base-resolution mapping of DNA methylation in single cells using single-cell bisulfite sequencing (scBS-seq). Nat Protoc. 2017;12(3):534-547.

22. Jing D, Huang Y, Liu X, et al. Lymphocyte-Specific Chromatin Accessibility Pre-determines Glucocorticoid Resistance in Acute Lymphoblastic Leukemia. Cancer Cell. 2018;34(6):906-921.

23. Yu CH, Wu G, Chang CC, et al. Sequential Approach to Improve the Molecular Classification of Childhood Acute Lymphoblastic Leukemia. J Mol Diagn. 2022;24(11):1195-1206.

24. Fang F, Lu J, Sang X, et al. Super-enhancer profiling identifies novel critical and targetable cancer survival gene LYL1 in pediatric acute myeloid leukemia. J Exp Clin Cancer Res. 2022;41(1):225.

25. Han C, Khodadadi-Jamayran A, Lorch AH, et al. SF3B1 homeostasis is critical for survival and therapeutic response in T cell leukemia. Sci Adv. 2022;8(3):eabj8357.

26. Zhu J, Tian Z, Li Y, et al. ATG7 Promotes Bladder Cancer Invasion via Autophagy-Mediated Increased ARHGDIB mRNA Stability. Adv Sci (Weinh). 2021;8(22):e2104365.

27. Zhang Y, Wang S, Zhang J, et al. Elucidating minimal residual disease of paediatric B-cell acute lymphoblastic leukaemia by single-cell analysis. Nat Cell Biol. 2022;24(2):242-252.

28. Zhang Y, Yu R, Li Q, et al. SNHG1/miR-556-5p/TCF12 feedback loop enhances the tumorigenesis of meningioma through Wnt signaling pathway. J Cell Biochem. 2020;121(2):1880-1889.

29. Luo Z, Li X, Zhao Z, Yang X, Xiao S, Zhou Y. MicroRNA-146a affects the chemotherapeutic sensitivity and prognosis of advanced gastric cancer through the regulation of LIN52. Oncol Lett. 2017;13(3):1386-1392.

30. An integrated encyclopedia of DNA elements in the human genome. Nature. 2012;489(7414):57-74.

31. Whyte WA, Orlando DA, Hnisz D, et al. Master transcription factors and mediator establish super-enhancers at key cell identity genes. Cell. 2013;153(2):307-319.

32. Hnisz D, Abraham BJ, Lee TI, et al. Super-enhancers in the control of cell identity and disease. Cell. 2013;155(4):934-947.

33. Wang Y, Song F, Zhang B, et al. The 3D Genome Browser: a web-based browser for visualizing 3D genome organization and long-range chromatin interactions. Genome Biol. 2018;19(1):151.

34. Wang X, Xu J, Zhang B, et al. Genome-wide detection of enhancer-hijacking events from chromatin interaction data in rearranged genomes. Nat Methods. 2021;18(6):661-668.

35. Mallard C, Johnston MJ, Bobyn A, et al. Hi-C detects genomic structural variants in peripheral blood of pediatric leukemia patients. Cold Spring Harb Mol Case Stud. 2022;8(1):a006157.

36. Jiang W, Zhou X, Li Z, et al. Prolyl 4-hydroxylase 2 promotes B-cell lymphoma progression via hydroxylation of Carabin. Blood. 2018;131(12):1325-1336.

37. Gao M, Wang J, Rousseaux S, et al. Metabolically controlled histone H4K5 acylation/acetylation ratio drives BRD4 genomic distribution. Cell Rep. 2021;36(4):109460.

38. Filippakopoulos P, Qi J, Picaud S, et al. Selective inhibition of BET bromodomains. Nature. 2010;468(7327):1067-1073.

39. Lovén J, Hoke HA, Lin CY, et al. Selective inhibition of tumor oncogenes by disruption of super-enhancers. Cell. 2013;153(2):320-334.

40. Baxter EW, Mirabella F, Bowers SR, et al. The inducible tissue-specific expression of the human IL-3/GM-CSF locus is controlled by a complex array of developmentally regulated enhancers. J Immunol. 2012;189(9):4459-4469.

41. De Braekeleer E, Douet-Guilbert N, Morel F, Le Bris MJ, Basinko A, De Braekeleer M. ETV6 fusion genes in hematological malignancies: a review. Leuk Res. 2012;36(8):945-961.

42. Aldoss I, Clark M, Song JY, Pullarkat V. Targeting the alpha subunit of IL-3 receptor (CD123) in patients with acute leukemia. Hum Vaccin Immunother. 2020;16(10):2341-2348.

43. Bulaeva E, Pellacani D, Nakamichi N, et al. MYC-induced human acute myeloid leukemia requires a continuing IL-3/GM-CSF costimulus. Blood. 2020;136(24):2764-2773.

44. Rossi Sebastiano M, Konstantinidou G. Targeting Long Chain Acyl-CoA Synthetases for Cancer Therapy. Int J Mol Sci. 2019;20(15):3624.

45. Chen WC, Wang CY, Hung YH, Weng TY, Yen MC, Lai MD. Systematic Analysis of Gene Expression Alterations and Clinical Outcomes for Long-Chain Acyl-Coenzyme A Synthetase Family in Cancer. PLoS One. 2016;11(5):e0155660.

46. Gilliland DG, Tallman MS. Focus on acute leukemias. Cancer Cell. 2002;1(5):417-420.

47. Shomali W, Gotlib J. World Health Organization-defined eosinophilic disorders: 2022 update on diagnosis, risk stratification, and management. Am J Hematol. 2022;97(1):129-148.

48. Francischetti IMB, Alejo JC, Sivanandham R, et al. Neutrophil and Eosinophil Extracellular Traps in Hodgkin Lymphoma. Hemasphere. 2021;5(9):e633.

49. Guo J, Zheng Q, Peng Y. BET proteins: Biological functions and therapeutic interventions. Pharmacol Ther. 2023;243:108354.

50. Ianevski A, Giri AK, Aittokallio T. SynergyFinder 2.0: visual analytics of multi-drug combination synergies. Nucleic Acids Res. 2020;48(W1):W488-W493.

Drug1	**Drug2**	**Synergy Score**
JQ1	Vincristine	24.93
ABBV-744	Vincristine	10.648
OTX015	Vincristine	10.916
I-BET 151	Vincristine	13.846
Mivebresib	Vincristine	13.124
PFI-1	Vincristine	21.124

Table 1. Combination index of different bromodomain and extraterminal domain (BET) inhibitors with vincristine.

Figures

Figure 1. *ETV6::ACSL6* dysregulates the ALL transcriptome and induces eosinophilia. (A) A representative image of bone marrow aspiration smear of an *ETV6::ACSL6* patient. The black arrow indicates eosinophils, and the red arrow indicates ALL cells. (B) Flow cytometry analysis displays eosinophils and ALL cells from bone marrow samples of the *ETV6::ACSL6* patient. The red population refer to ALL cells. (C) Volcano plot showing upregulated and downregulated genes in ALLs and eosinophils compared to a healthy control. Vertical dashed lines, cutoff of 1.5-fold changes; horizontal dashed lines, cutoff at p value = 0.05. Eos, eosinophils. NoSignifi, not significant. (D) Fold changes of *IL-3* and *IL-5* expression in an *ETV6::ACSL6* patient compared with a healthy control (n = 3). RJ-9, an *ETV6::ACSL6* ALL patient. $^{*}p < 0.05$, $^{**}p < 0.01$. (E, F) Hierarchical clustering of gene expression profiles of *ETV6::ACSL6* ALL in comparison with eosinophils and ALLs of various subtypes. E showed all the genes detected. F focused on genes nearby the *ETV6*::*ACSL6* junction at chr5 and chr12. Chr5 and chr12 are each split into two segments, with the upper portion indicating genes downstream of the breakpoint and the lower portion indicating genes upstream of the breakpoint. Each row corresponds to a gene. HD, healthy donor.

Figure 2. Multi-omics analysis of *ETV6::ACSL6* ALL cells.

(A) Mapping of chromosomal breakpoints by RNA-seq revealed a fusion of the first exon of *ETV6* to the second exon of *ACSL6*. (B) DNA sequences nearby the breakpoints on chr12 and chr5 in *ETV6::ACSL6* ALL determined using ONT sequencing. Breakpoints on chr12 and chr5 are indicated by the arrow, and the coordinates are showed. The sequence of 20 base pairs near the breakpoints are also displayed. *IL-3* locus is located at the minus strand of the translocated chromosome. (C) RNA-seq data showed a fusion of *ETV6* and *ACSL6* genes. Black bar, *ETV6::ACSL6* fusion with highest statistical confidence; Gray bars, other fusion events with unsignificant statistical confidence; green bar, duplication; blue bar, inversion. (D) Schematic diagram of *ETV6::ACSL6* mRNA splicing. The ONT data and RNA-seq data display the fusion gene at the DNA and RNA levels respectively. Grey bars, introns; pink bar, exon 1 of *ETV6*; purple bar, exon 1 of *ACSL6*; blue bars, exons 2-21 of *ACSL6*; e1, exon 1; e2-21, exon 2 to 21 of *ACSL6*. (E) Structural variants identified by ONT sequencing. Black bold line, *ETV6::ACSL6* translocation with highest confidence (VAF = 0.9). The other three interchromosomal lines are unbalanced translocations. Purple line in the circle, insertion; Black line in the circle, deletion; Red line in the circle, inversion; Blue line in the circle, duplication. (F) UMAP projection analysis of single-cell RNA-seq on ALLs and eosinophils. Pink dots, ALL cells; Blue dots, eosinophils. (G) GSEA of differentially expressed genes between ALLs and eosinophils. (H) Left, single-cell methylation data at *IL-3* loci. Right, single-cell accessibility data at *IL-3* loci. Since cytosines in GpCs at open chromatin regions were arbitrarily methylated by adding GpC methyltransferase before bisulfite conversion, the methylated GpC is considered to represent accessible chromatin. Bar plot showing the average level of all cells detected at indicated genomic loci. Each row in the box corresponds to a single cell. Each dot represents the methylation or accessibility level of the corresponding cell (horizontally) at the corresponding genomic position (vertically). RJ-9, an *ETV6::ACSL6* ALL patient.

Figure 3. Enhancer hijacking events occur in *ETV6::ACSL6* ALL

(A) Heatmap of super-enhancer abundance of 32 hematopoietic and 54 non-hematopoietic cell types from the ENCODE database. Red, detection of super-enhancer in the corresponding cell type, purple, not detected. Each column represents a cell type, each row represents a super-enhancer coordinate. (B) CUT&Tag profiles for epigenetic marks at the *ETV6* locus in the *ETV6::ACSL6* RJ-9 ALL, ALL50 and control datasets from ENCODE database. Gray line highlights the breakpoint detected by ONT sequencing. Green line highlights the promoter of *ETV6*. Yellow bar highlights the main region of *ETV6*-SE. ALL50, a normal karyotype ALL patient. ENCODE: GM12878, H1-hESC, K562. (C) Ranking of super-enhancers by analyzing H3K27ac datasets of an *ETV6::ACSL6* patient sample using ROSE algorithm. (D) CUT&Tag profiles of H3K27ac at the *ETV6* locus in Nalm6 and REH cell lines. Nalm6, a Pre-B ALL cell line with *ETV6::PDGFR* translocation. REH, Pre-B ALL cell line with *ETV6::RUNX1* translocation. Yellow shading highlights the *ETV6*-SE identified in the *ETV6::ACSL6* sample. (E) *ETV6* and its promoter region are separated into two parts by the breakpoint. Green rectangle, Pro-SE1(Promoter and left section of *ETV6*), blue rectangle, SE2 (right section of *ETV6*). For the luciferase reporter assay, regions from both Pro-SE1 and SE2 were selected based on TF binding and DNase accessibility from ENCODE as indicated in orange shading. (F)

Schematic depicting the luciferase reporter construct. (G) Luciferase reporter assay. Selected elements in (E) were cloned into a luciferase reporter plasmid pGL3p. The fold inductions were calculated by normalizing to pGL3p control. Statistical significance was calculated using two-tailed t-tests. Data represent the mean ± SEM of 3 biological replicates. $^{*}p < 0.05$, $^{****}p < 0.0001$. (H) Transcription factor binding site analysis (MEME) of the *ETV6* super-enhancer. The transcription factors were ranked by *p*-value, and the top five transcription factors are listed.

Figure 4. *ETV6::ACSL6* induces changes of chromatin conformation.

(A) Visualization of Hi-C data with Juicebox. Dotted circles indicate an interaction between chr5 and chr12. RJ-9, an *ETV6::ACSL6* ALL patient. (B, C) Hi-C data from *ETV6::ACSL6* ALL patient (RJ-9) in comparison with GM12878. Blue dotted lines refer to the interaction between SE2 with target genes, and gray shaded regions indicate the region with stronger interaction. Green dotted lines refer to interactions between Pro-SE1 and target genes. RNA-seq and H3K27ac CUT&Tag coverage are shown below the Hi-C data. Dotted lines indicate the breakpoint on chr12 and chr5. (D) Hi-C maps of rearranged chromosomes EA and IE. Black arrows and dashed triangles refer to newly formed TADs. Pro-SE1 and SE2 are indicated in green and blue rectangles. Pink bar, chr12; blue bar, chr5. CTCF CUT&Tag coverage is shown below the Hi-C map. Yellow shading highlights CTCF binding boundaries. Vertical dashed lines represent the breakpoint on chr12 and chr5. (E) Gene expression profiles within the newly formed TADs at EA and IE. Black boxes show genes located within the TADs involving Pro-SE1 or SE2.

Figure 5. BETi has the potential to reverse molecular changes caused by the *ETV6* translocation

(A) A heatmap represents the relative expression levels of genes following 1μM JQ1 treatment for 24h. Fold change of gene expression under treatment conditions over the control (DMSO) is shown. Exemplary genes are annotated. Each row corresponds to a gene. (B) Volcano plot showing upregulated (right part) or downregulated (left part) following 1μM JQ1 treatment for 24h compared with DMSO. (C) GSEA analysis of DMSO (left) and JQ1 treatment (right). The differentially expressed genes of two groups were ranked according to their log10 (*p* value). (D) Downregulation of *IL-3* RNA level by JQ1. *ETV6::ACSL6* ALL cells (2×10^{6} cells) were treated with JQ1 in a time and concentration dependent manner. Hrs, hours. (E) IL-3 concentration in the cell culture supernatant following 1μM JQ1 treatment for 24 h. RJ-9, an *ETV6::ACSL6* ALL patient. RJ-13, an *ETV6::RUNX1* ALL patient. (F) BRD4 occupancy at the *ETV6* gene locus in JQ1 and DMSO treated samples as determined by CUT&Tag. (G) BRD4 enrichment at the *ETV6* locus as determined by CUT&Tag after DMSO (left) or 1μM JQ1 treatment for 24h. The *y* axis shows BRD4 CUT&Tag signal in units of rpm/bp. (H) Genome-wide BRD4 binding level after 1μM JQ1 treatment for 24h as identified by CUT&Tag. (I) Distribution of genomic elements associated BRD4 peaks following JQ1 treatment. Ctrl, control. BETi, the bromodomain and extraterminal domain inhibitors.

Figure 6. Effects of BETi on *ETV6::ACSL6* ALL *in vitro* and *in vivo*.

(A) Cytotoxicity assay on ALL patient cells with various karyotype. Cells were treated with the indicated concentrations of JQ1. Data represent the mean ± SEM of 3 biological replicates. ****, $p < 0.0001$. RJ-9, *ETV6::ACSL6*. RJ-13, *ETV6::RUNX1*. RJ-14, *BCR::ABL1*. RJ-15, normal karyotype. (B) Synergistic effect of JQ1 and vincristine in inhibiting cell viability of RJ-9 cells. ZIP, ZIP synergy score(50). (C) Cytotoxic assay of JQ1 and vincristine at indicated concentrations. ****$p < 0.0001$. (D) A schematic diagram of *in vivo* drug administration. BM cells from the *ETV6::ACSL6* patient were harvested and transplanted into NSG mice, which were then treated with JQ1(50 mg/kg, i.p., five days a week) and vincristine (0.5 mg/kg, i.p., five days a week), separately or in combination for four weeks. Leukemia burden in the peripheral blood was monitored over time until relapse. After humanely killing the mice, the bone marrows and spleens were preserved as mononuclear cells for further use. (E) RNA levels of *IL-3* in different groups after *in vivo* treatment for 24h (measured via RT-PCR, n=3). n.s., not significant (one-way ANOVA with all samples compared with vehicle control). (F) Assessment of leukemia burden in spleen, bone marrow and peripheral blood in an *in vivo* RJ-9 PDX model after 28 days treatment with vincristine (n=4) and combination treatments of JQ1 and vincristine (n=4). Data are represented as a percentage of hCD45$^+$ cells for each experiment and expressed as the mean ± SEM; *$p < 0.05$; ***$p < 0.001$ by Mann-Whitney U test. (G) Leukemia burden in the peripheral blood over time. (H) Kaplan-Meier curves for event-free survival are shown for vehicle control (n=7), vincristine (n=6), JQ1 (n=5), and combination treatments (n=4) against RJ-9 PDX *in vivo*. Event, % hCD45$^+$ cells = 25%. ****p < 0.0001. by Gehan-Breslow-Wilcoxon test. BETi, the bromodomain and extraterminal domain inhibitors.

Figure 1

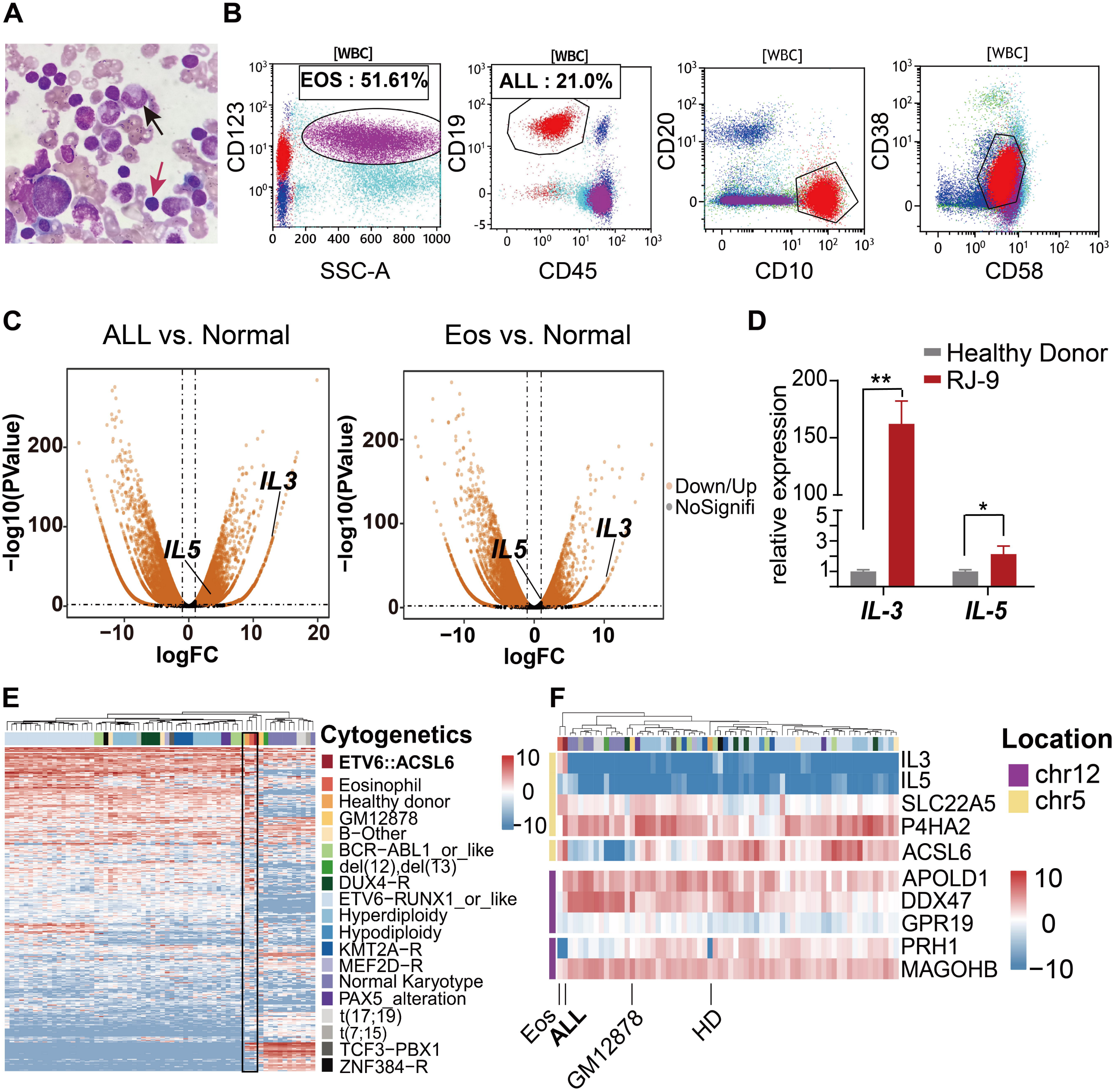
A
B
[WBC]
EOS : 51.61%
CD123
SSC-A
0
200
400
600
800
1000
[WBC]
ALL : 21.0%
CD19
CD45
[WBC]
CD20
CD10
[WBC]
CD38
CD58
C
ALL vs. Normal
Eos vs. Normal
-log10(PValue)
logFC
IL3
IL5
Down/Up
NoSignifi
D
Healthy Donor
RJ-9
relative expression
**
*
IL-3
IL-5
E
Cytogenetics
ETV6::ACSL6
Eosinophil
Healthy donor
GM12878
B-Other
BCR-ABL1_or_like
del(12),del(13)
DUX4-R
ETV6-RUNX1_or_like
Hyperdiploidy
Hypodiploidy
KMT2A-R
MEF2D-R
Normal Karyotype
PAX5_alteration
t(17;19)
t(7;15)
TCF3-PBX1
ZNF384-R
F
10
0
-10
IL3
IL5
SLC22A5
P4HA2
ACSL6
APOLD1
DDX47
GPR19
PRH1
MAGOHB
Location
chr12
chr5
Eos
ALL
GM12878
HD

Figure 2

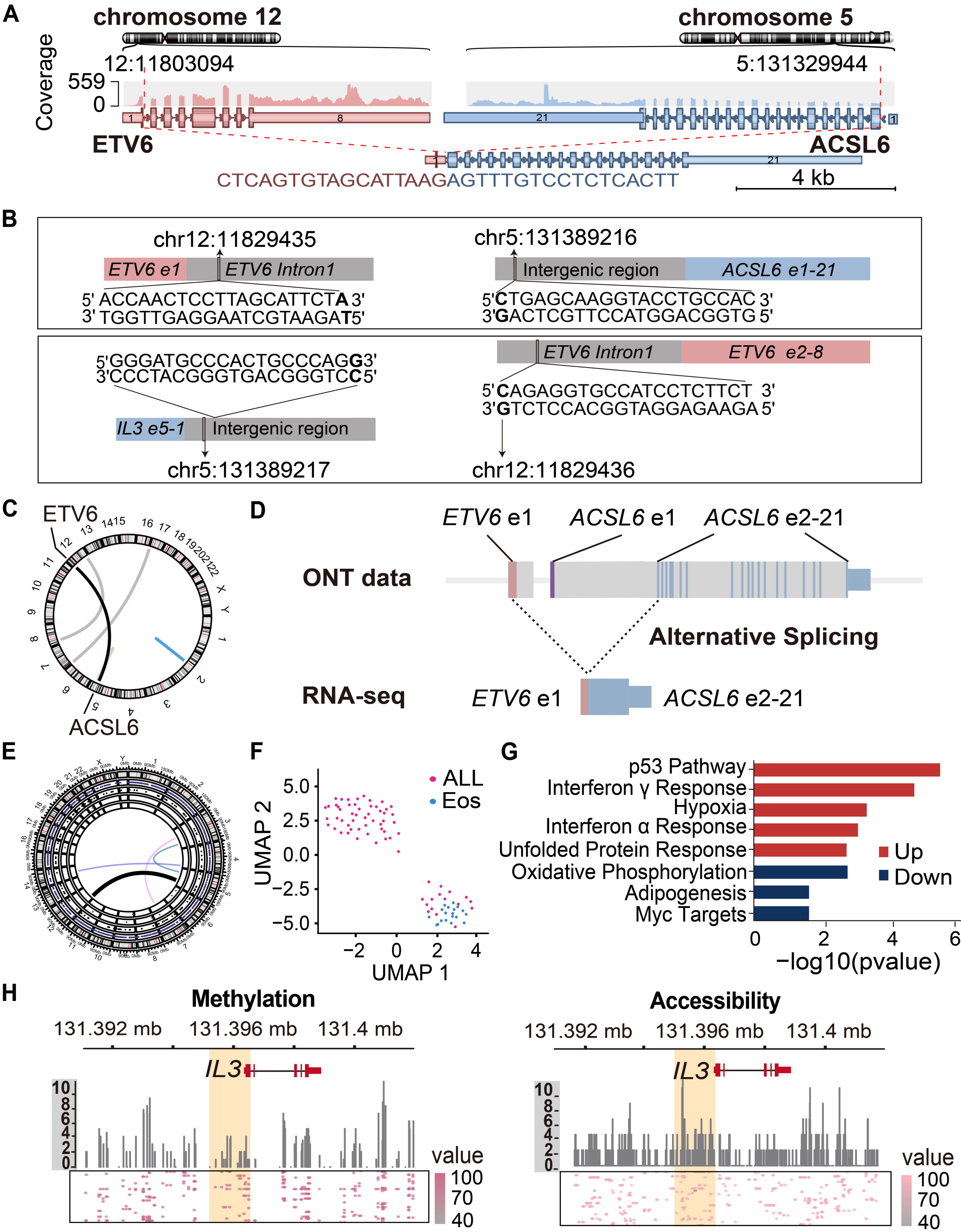
A
chromosome 12
chromosome 5
Coverage
559
0
12:11803094
5:131329944
1
8
21
1
ETV6
ACSL6
1
21
CTCAGTGTAGCATTAAGAGTTTGTCCTCTCACTT
4 kb
B
chr12:11829435
ETV6 e1
ETV6 Intron1
5' ACCAACTCCTTAGCATTCTA 3'
3' TGGTTGAGGAATCGTAAGAT 5'
chr5:131389216
Intergenic region
ACSL6 e1-21
5' CTGAGCAAGGTACCTGCCAC 3'
3' GACTCGTTCCATGGACGGTG 5'
5' GGGATGCCCACTGCCCAGG 3'
3' CCCTACGGGTGACGGGTCC 5'
IL3 e5-1
Intergenic region
chr5:131389217
ETV6 Intron1
ETV6 e2-8
5' CAGAGGTGCCATCCTCTTCT 3'
3' GTCTCCACGGTAGGAGAAGA 5'
chr12:11829436
C
ETV6
ACSL6
D
ETV6 e1
ACSL6 e1
ACSL6 e2-21
ONT data
Alternative Splicing
RNA-seq
ETV6 e1
ACSL6 e2-21
E
F
ALL
Eos
UMAP 2
UMAP 1
5.0
2.5
0.0
−2.5
−5.0
−2
0
2
4
G
p53 Pathway
Interferon γ Response
Hypoxia
Interferon α Response
Unfolded Protein Response
Oxidative Phosphorylation
Adipogenesis
Myc Targets
Up
Down
0
2
4
6
−log10(pvalue)
H
Methylation
131.392 mb
131.396 mb
131.4 mb
IL3
10
8
6
4
2
0
value
100
70
40
Accessibility
131.392 mb
131.396 mb
131.4 mb
IL3
10
8
6
4
2
0
value
100
70
40

Figure 3

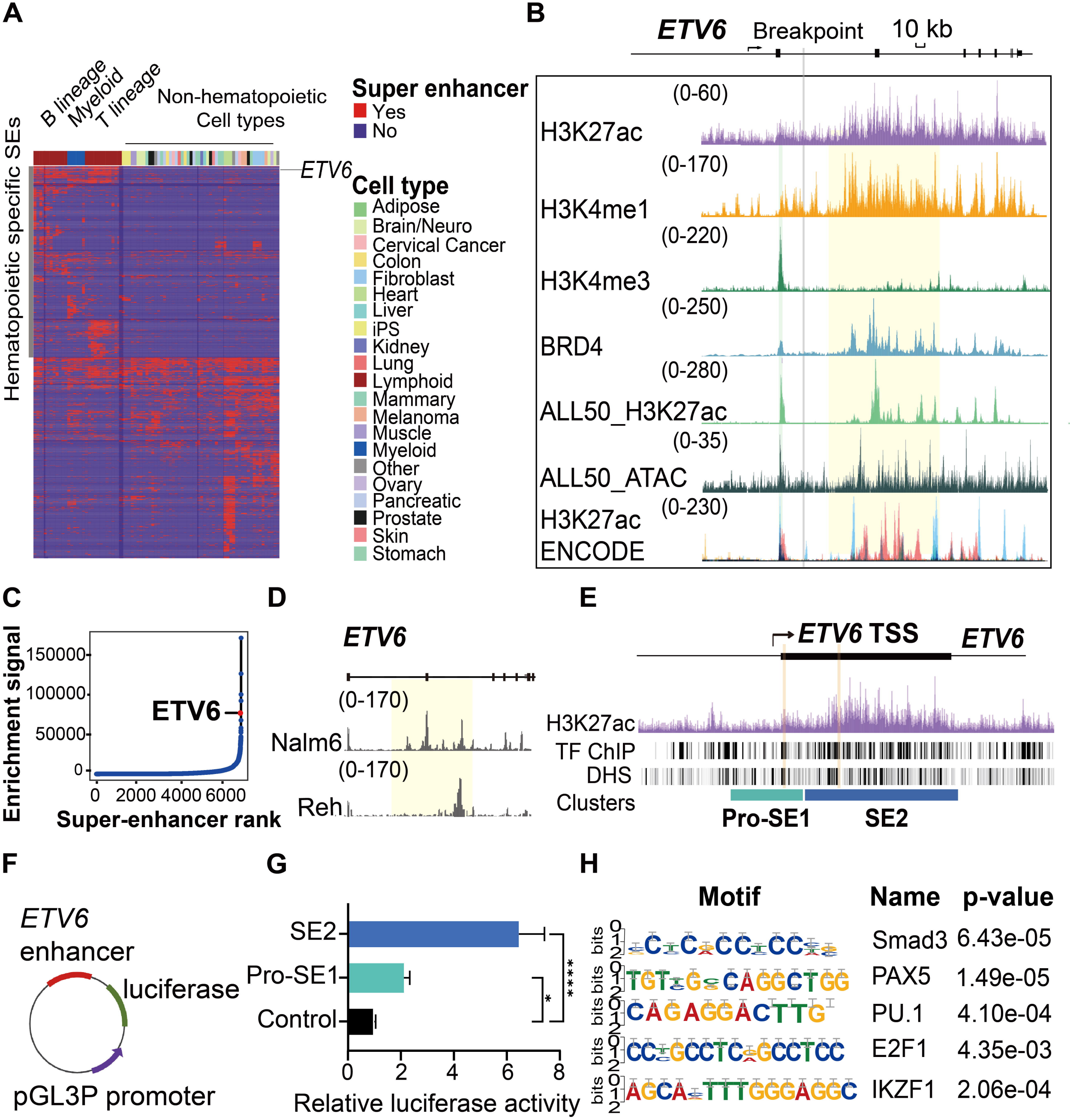
A
B lineage
Myeloid
T lineage
Non-hematopoietic
Cell types
Hematopoietic specific SEs
ETV6
Super enhancer
Yes
No
Cell type
Adipose
Brain/Neuro
Cervical Cancer
Colon
Fibroblast
Heart
Liver
iPS
Kidney
Lung
Lymphoid
Mammary
Melanoma
Muscle
Myeloid
Other
Ovary
Pancreatic
Prostate
Skin
Stomach
B
ETV6
Breakpoint
10 kb
(0-60)
H3K27ac
(0-170)
H3K4me1
(0-220)
H3K4me3
(0-250)
BRD4
(0-280)
ALL50_H3K27ac
(0-35)
ALL50_ATAC
(0-230)
H3K27ac
ENCODE
C
Enrichment signal
150000
100000
50000
0
ETV6
0
2000
4000
6000
Super-enhancer rank
D
ETV6
(0-170)
Nalm6
(0-170)
Reh
E
ETV6 TSS
ETV6
H3K27ac
TF ChIP
DHS
Clusters
Pro-SE1
SE2
F
ETV6
enhancer
luciferase
pGL3P promoter
G
SE2
Pro-SE1
Control
****
*
0
2
4
6
8
Relative luciferase activity
H
Motif
Name
p-value
bits
Smad3
6.43e-05
PAX5
1.49e-05
PU.1
4.10e-04
E2F1
4.35e-03
IKZF1
2.06e-04

Figure 4

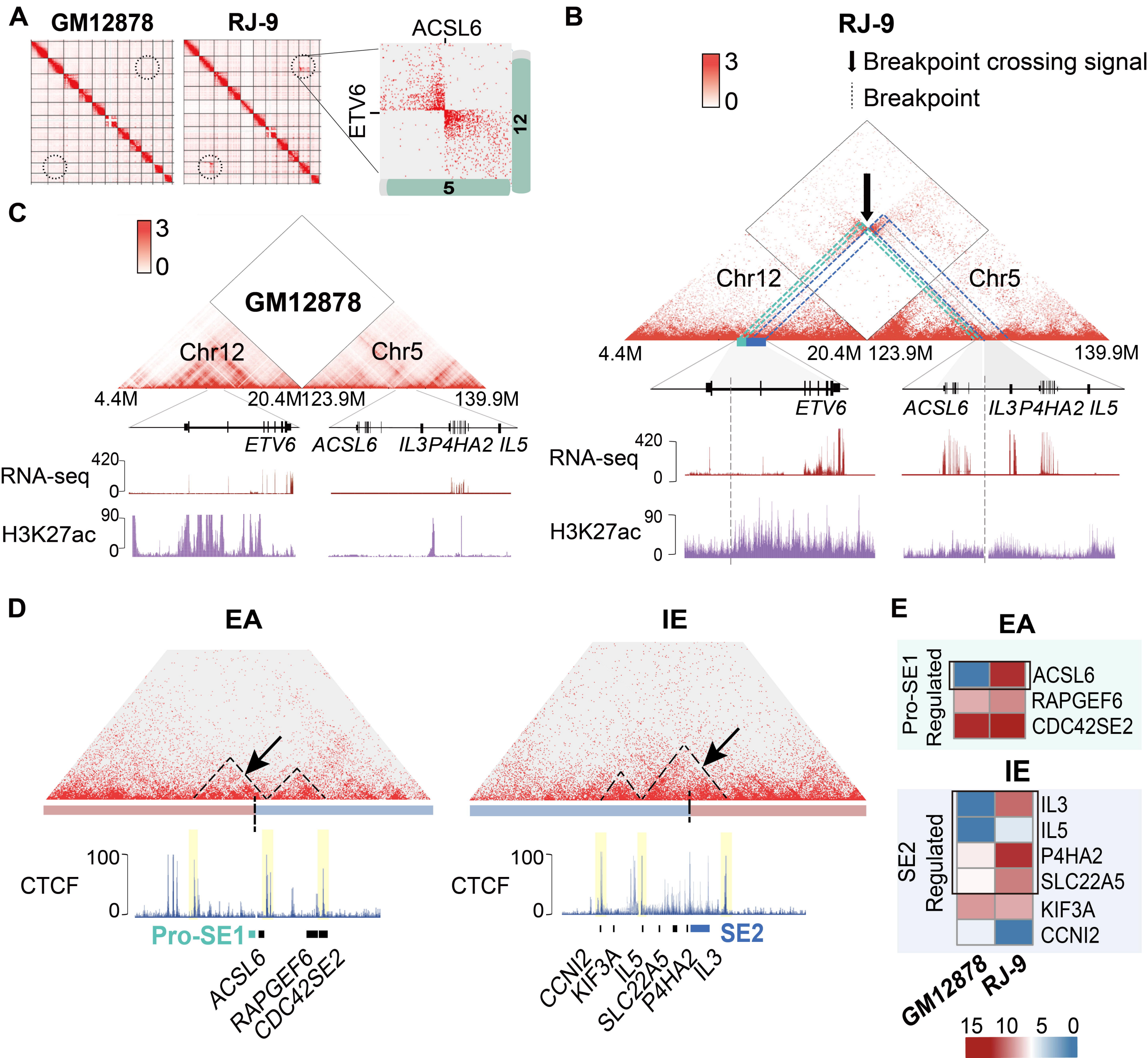
A
GM12878
RJ-9
ACSL6
ETV6
12
5
B
RJ-9
3
0
Breakpoint crossing signal
Breakpoint
Chr12
Chr5
4.4M
20.4M
123.9M
139.9M
ETV6
ACSL6
IL3
P4HA2
IL5
RNA-seq
420
0
H3K27ac
90
0
C
3
0
GM12878
Chr12
Chr5
4.4M
20.4M
123.9M
139.9M
ETV6
ACSL6
IL3
P4HA2
IL5
RNA-seq
420
0
H3K27ac
90
0
D
EA
IE
CTCF
100
0
Pro-SE1
ACSL6
RAPGEF6
CDC42SE2
CTCF
100
0
SE2
CCNI2
KIF3A
IL5
SLC22A5
P4HA2
IL3
E
EA
Pro-SE1 Regulated
ACSL6
RAPGEF6
CDC42SE2
IE
SE2 Regulated
IL3
IL5
P4HA2
SLC22A5
KIF3A
CCNI2
GM12878
RJ-9
15
10
5
0

Figure 5

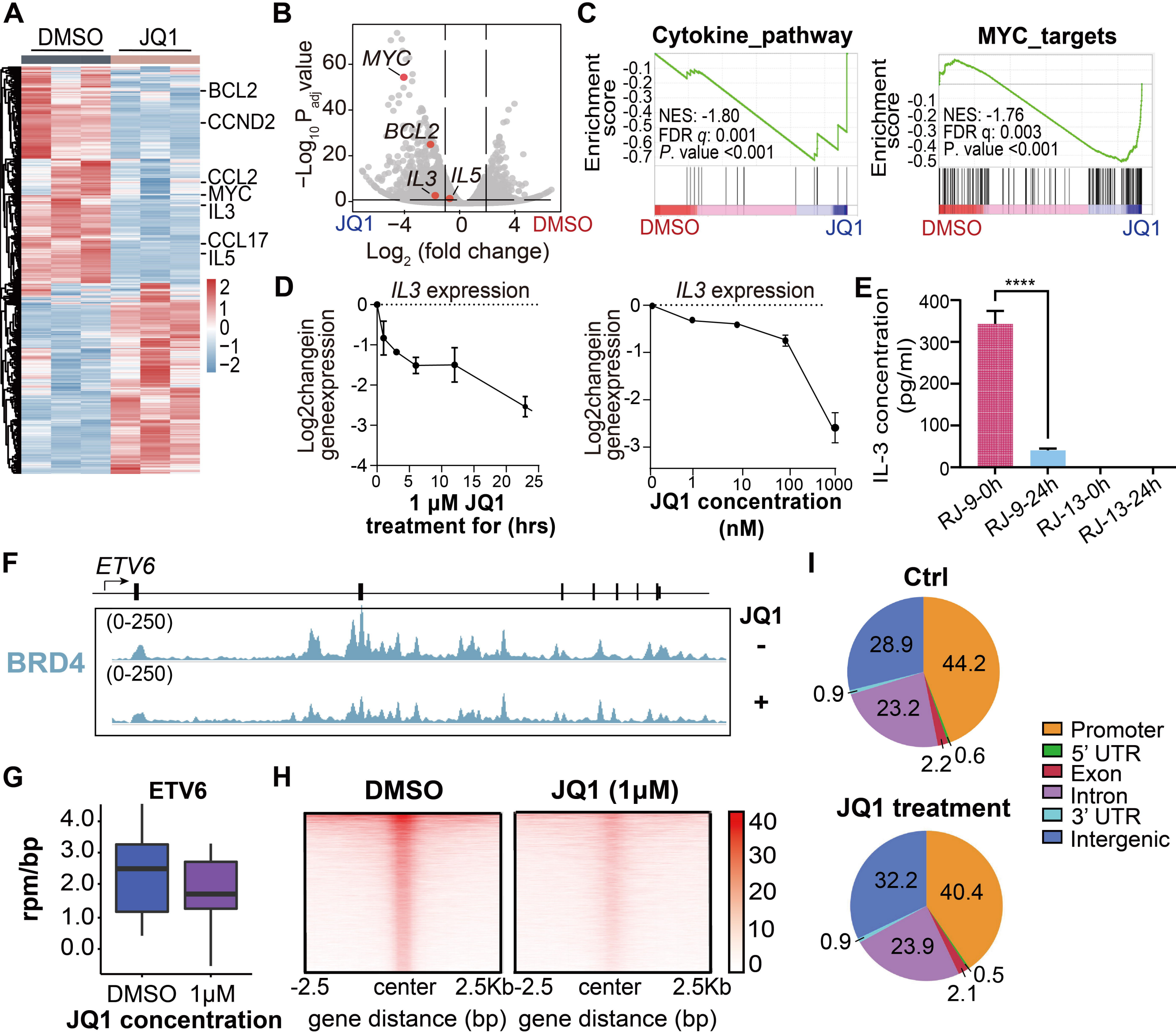
A
DMSO
JQ1
BCL2
CCND2
CCL2
MYC
IL3
CCL17
IL5
2
1
0
−1
−2
B
−Log10 Padj value
60
40
20
0
MYC
BCL2
IL3
IL5
JQ1
−4
0
4
DMSO
Log2 (fold change)
C
Cytokine_pathway
Enrichment score
-0.1
-0.2
-0.3
-0.4
-0.5
-0.6
-0.7
NES: -1.80
FDR q: 0.001
P. value <0.001
DMSO
JQ1
MYC_targets
Enrichment score
-0.1
-0.2
-0.3
-0.4
-0.5
NES: -1.76
FDR q: 0.003
P. value <0.001
DMSO
JQ1
D
IL3 expression
Log2changein geneexpression
0
-1
-2
-3
-4
0
5
10
15
20
25
1 μM JQ1 treatment for (hrs)
IL3 expression
Log2changein geneexpression
0
-1
-2
-3
0
1
10
100
1000
JQ1 concentration (nM)
E
IL-3 concentration (pg/ml)
400
300
200
100
0
****
RJ-9-0h
RJ-9-24h
RJ-13-0h
RJ-13-24h
F
ETV6
BRD4
(0-250)
(0-250)
JQ1
-
+
G
ETV6
rpm/bp
4.0
3.0
2.0
1.0
0.0
DMSO
1μM
JQ1 concentration
H
DMSO
JQ1 (1μM)
40
30
20
10
0
-2.5
center
2.5Kb
-2.5
center
2.5Kb
gene distance (bp)
gene distance (bp)
I
Ctrl
28.9
44.2
0.9
23.2
2.2
0.6
JQ1 treatment
32.2
40.4
0.9
23.9
2.1
0.5
Promoter
5' UTR
Exon
Intron
3' UTR
Intergenic

Figure 6

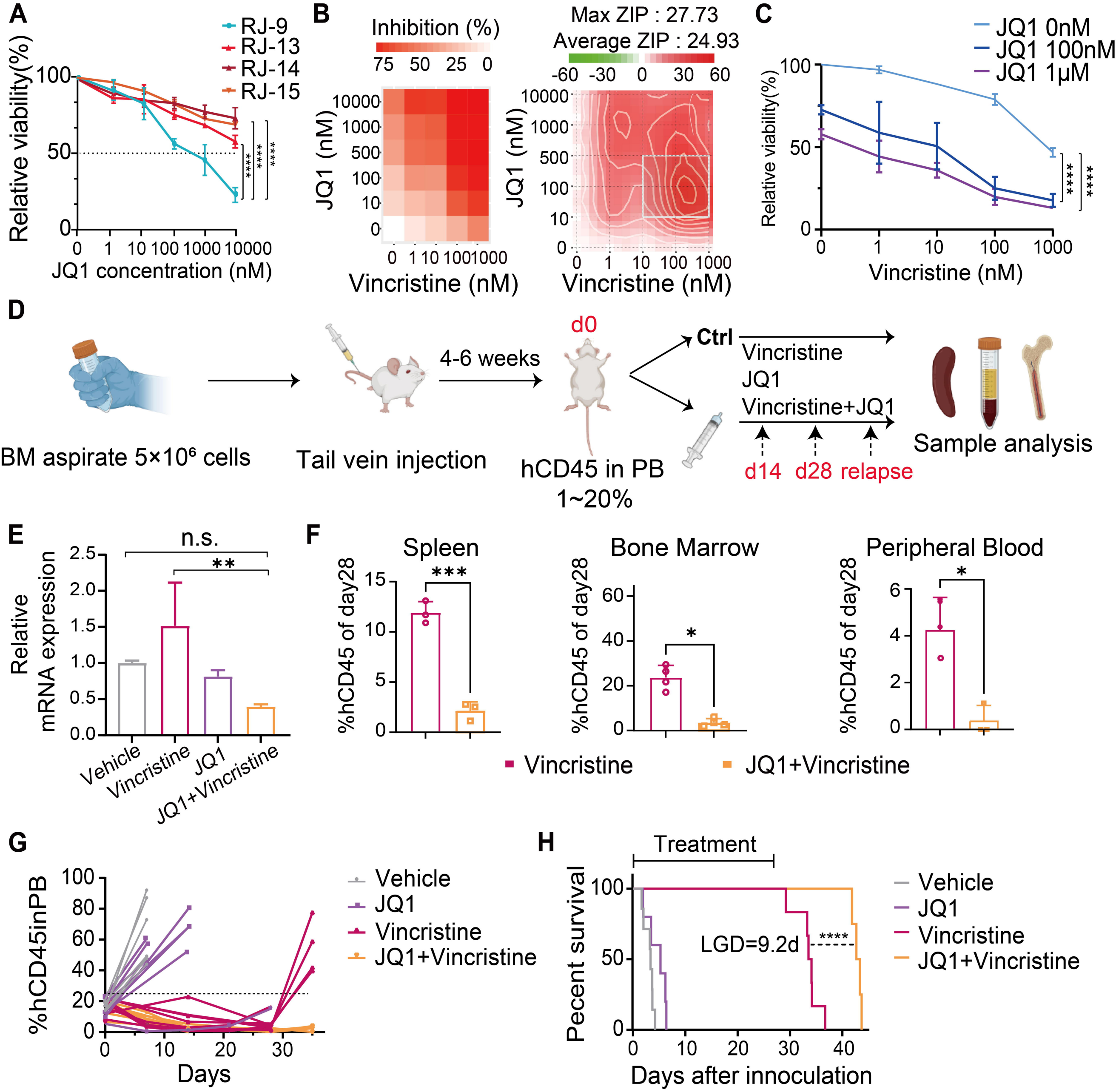
A
RJ-9
RJ-13
RJ-14
RJ-15
Relative viability(%)
100
50
0
0 1 10 100 1000 10000
JQ1 concentration (nM)
****
****
****
B
Inhibition (%)
75 50 25 0
JQ1 (nM)
10000
1000
500
100
10
0
0 1 10 100 1000
Vincristine (nM)
Max ZIP : 27.73
Average ZIP : 24.93
-60 -30 0 30 60
JQ1 (nM)
10000
1000
500
100
10
0
0 1 10 100 1000
Vincristine (nM)
C
JQ1 0nM
JQ1 100nM
JQ1 1μM
Relative viability(%)
100
50
0
0 1 10 100 1000
Vincristine (nM)
****
****
D
BM aspirate 5×10⁶ cells
Tail vein injection
4-6 weeks
d0
hCD45 in PB
1~20%
Ctrl
Vincristine
JQ1
Vincristine+JQ1
d14
d28
relapse
Sample analysis
E
Relative
mRNA expression
2.5
2.0
1.5
1.0
0.5
0.0
n.s.
**
Vehicle
Vincristine
JQ1
JQ1+Vincristine
F
Spleen
%hCD45 of day28
15
10
5
0
***
Bone Marrow
%hCD45 of day28
60
40
20
0
*
Peripheral Blood
%hCD45 of day28
6
4
2
0
*
Vincristine
JQ1+Vincristine
G
%hCD45inPB
100
80
60
40
20
0
0 10 20 30
Days
Vehicle
JQ1
Vincristine
JQ1+Vincristine
H
Treatment
Pecent survival
100
50
0
0 10 20 30 40
Days after innoculation
LGD=9.2d
****
Vehicle
JQ1
Vincristine
JQ1+Vincristine

Supplementary Tables

The following tables were uploaded as individual Excel files.

Supplementary Table S1: List of SVs detected by ONT sequencing

Description of all SVs detected in the *ETV6::ACSL6* ALL cells, including the chromosome position, variation type, reference sequence, variant sequence, overall information and Variant Allele Frequency (VAF) for each SV. INS, insertion; DEL, deletion; INV, inversion; DUP, duplication; BND, breakend.

Supplementary Table S2: Genetic aberrations and functional annotations by RNA sequencing and ONT sequencing

Lists of recurrent leukemia-associated mutations detected by RNA-seq as well as the functional annotation of somatic SVs detected by ONT sequencing. In the left "RNA sequencing" section, we listed the results of some recurrent gene variations in leukemia. In the right "ONT sequencing" section, we showed the somatic SVs after filtering out germline variations, including variation types, chromosomal positions, VAF values, functional regions, and their adjacent genes.

Supplementary Table S3: Patient information

Description of ALL patients in the study. Bone marrow samples from five B-ALL patients were used in the study. The table showed their basic information, including gender, age at diagnosis, diagnosis date, initial white blood cell count, cytogenetics, and risk stratification.

Supplementary Methods

Nanopore long-read sequencing

High-molecular-weight (HMW) DNA was extracted from *ETV6::ACSL6* ALL cells with the MagAttract HMW DNA kit (Qiagen; 67563) according to the manufacturer's instructions. Briefly, 1×10^7 frozen cells were lysed with 200 μL of buffer ATL and 20 μL of proteinase K and incubated overnight at 56 °C and 900 r.p.m. 4 μL of RNase A was added to cleave RNA. 150 μL of buffer AL, 280 μL of buffer MB, and 40 μL of MagAttract Suspension G beads were then added to capture the HMW DNA. Next, the beads were cleaned up with 700 μL of buffer MW1, buffer PE, and NFW and eluted with 200 μL of buffer AE. The HMW was sequenced on a MinION Mk1b device (ONT).

Read sequences were extracted from base-called FAST5 files by Poretools (version 0.5.1) to generate a FASTQ file. Raw reads were aligned to hg38 with minimap2 (version 2.24). Structural variants were called using cuteSV (version 1.0.8) and Sniffles2 (version 2.0.7). Filtering steps of structural variants are described below: (1) Structural variants (chr1-22, X, and Y) with Allele Frequency > 0.3, Reads >= 10, and marked as PRECISE were included using snpSift (version 5.1d); (2) After depth information was added to individual structural variant by uphold (version 0.2.3), deletions with DHFFC > 0.7 and duplications with DHBFC <1.3 were excluded by bcftools (version 1.9); (3) Structural variants from different callers were merged by SURVIVOR (version 1.0.7); (4) Insertions and deletions in the merged call set overlapping with Simple repeat and Microsatellite regions from UCSC genome browser were removed by bedTools (version 2.30.0); (5) All structural variants in the merged call set overlapping with gnomAD structural variants were removed by bedTools (version 2.30.0). Genomic coordinates (hg19 to hg38) of gnomAD structural variants were lifted over using CrossMap (version 0.6.3).

RNA-seq

Total RNA was extracted and reverse transcribed using Yeasen. The cDNA was synthesized and added with adaptors. The amplified sample libraries were then paired-end sequenced (2×150 bp) on the Novaseq 6000 system and aligned against the human genome (hg19). Other ALL datasets were generated from previous publications(1-3) (accession no. GSE57795, GSE207057, and GSE164072).

Hi-C Sequencing

Hi-C was performed using a modified version of a previously described protocol(4). Cells were crosslinked with formaldehyde, and DNA was digested with MboI (NEB, R0147) that leaves a 5′overhang; the 5′overhang was filled, including a biotinylated residue; and the resulting blunt-end fragments were ligated under dilute conditions that favor ligation events between the cross-linked DNA fragments. The resulting DNA sample contained ligation products consisting of fragments that were originally in close spatial proximity in the nucleus, marked with biotin at the junction. A Hi-C library was created by shearing the DNA and selecting the biotin-containing fragments with streptavidin beads. The library was then analyzed by using massively parallel DNA sequencing.

CUT&Tag library preparation

CUT&Tag assays were performed as described previously(5). In brief, approximately

10,000 PDX cells in each biological replicate were harvested and centrifuged (400 × g) at room temperature for 5 min. The supernatant was washed and resuspended in Wash Buffer supplemented with protease inhibitors (Sigma). Concanavalin A-coated magnetic beads in each sample were washed and resuspended in binding buffer. Then beads were added to the cells, gently vortexed, and incubated in a shaker for 10 min at room temperature. The unbound supernatant was removed. The bead-bound cells were resuspended in precooling antibody buffer [2 mM EDTA, 0.1% BSA in DIG Wash Buffer (0.05% digitonin in wash buffer)] and incubated with (1:50 dilution) primary antibody against H3K27ac (ab177178, Abcam), H3K4me1 (ab176877, Abcam), H3K4me3 (ab213224, Abcam), p300 (ab275378, Abcam) and BRD4 (ab128874, Abcam) in a shaker overnight at 4°C. The primary antibody on the magnet stand was removed, and then a secondary antibody (Goat Anti-Rabbit IgG antibody, Vazyme) was diluted (1:100) in DIG Wash buffer and incubated with cells at room temperature for 1 h. Cells were washed in DIG Wash buffer using the magnet stand to remove unbound antibodies. A dilution of hyperactive pA-Tn5 transposon complex (0.04 μM) was prepared in DIG-300 buffer supplemented with 0.01% digitonin and protease inhibitors. Then cells were incubated with pA-Tn5 transposon complex in a shaker at room temperature for 1 h. Subsequently, cells were resuspended in tagmentation buffer (10 mM MgCl2 in DIG-300 buffer) and incubated at 37°C for 1 h. To terminate tagmentation, we added 10 μl of 0.5 M EDTA, 3 μl of 10% SDS, and 2.5 μl of 20 mg/ml proteinase K to each sample, followed by overnight incubation at 37°C. Purified DNA was amplified and indexed. The libraries were cleaned using Agencourt AMPure XP (Beckman) and sequenced on the Illumina Novaseq 6000 (Illumina). We applied 150-bp pair-end sequencing with a sequencing depth of 6G base pair raw data (generated approximately 20 million mapped paired reads).

Overexpression of *ETV6::ACSL6*

Human *ETV6::ACSL6* fusion cDNA was cloned into a lentiviral expression vector (GL121, pSLenti-EF1-EGFP-CMV-MCS-WPRE). Cells were transduced with lentivirus and then sorted to obtain GFP$^+$ cells.

Cytotoxicity Assays

PDX cells were seeded in 96-well U bottomed plates at 3,500,00 cells per 100 μl medium per well. JQ1 (Selleck) or vehicle control was added in triplicate wells. The cells in triplicate wells were incubated for a series of time points. Following the incubation, cck8 reagent (Yeasen) was added. After an additional 4 h incubation, fluorescence was measured, and cell viability was expressed relative to vehicle-treated control cells. The additive effect of combination treatment (drugs 1 and 2) was calculated as: [relative survival fraction drug 1×relative survival fraction drug 2]. The *p* values were calculated by comparing the combination treatment to the presumed additive effect at each time point.

Cytometric Beads Array for Detecting Cytokines Levels

The level of IL-3, IL-5, and GM-CSF in the supernatant of cultured Nalm6 cells was determined using Cytometric Beads Array (BD Pharmingen) according to the manufacturer's instructions. Data were acquired on FACS Aria-II (BD Bioscience). Data were analyzed using FCAP Array software (BD Bioscience).

Luciferase Reporter Assay

The luciferase reporter assay was performed using pGL3P vectors from Promega (Madison, Wisconsin, USA), and luminescence was detected using the Dual-Glo system from Vazyme. Gene enhancer sequences were synthesized as dsDNA by IDT. The dsDNA was inserted into the pGL3P vector between Sal1 and BamH1 cutting sites, which is 1 kb downstream of the 3' end of the firefly luciferase gene. The cloned vector was co-transfected with pRL-TK renilla luciferase control reporter vectors (Promega) into 293T cells. The firefly and renilla luminescence were detected in the transfected cells after 24 hours of transfection using the Dual-Glo Luciferase Assay System (Vazyme). The firefly luminescence was normalized to renilla luminescence for each condition. Fold inductions were then calculated by normalizing to pGL3P control.

Western blotting

Radio immunoprecipitation (RIPA) lysis buffer (Yeasen) was used for the lysing of Nalm6 cells. Cell lysates were subjected to 12.5% SDS-polyacrylamide gel electrophoresis and transferred onto polyvinylidene difluoride membranes. Then, the membranes were incubated with the indicated antibodies. Primary antibodies against ETV6, flag, IL3, and GAPDH were purchased from Abcam. The secondary antibodies conjugated with HRP were used at 1:2,000 dilutions (CST). The protein bands were detected with the enhanced chemiluminescence reagent.

Hi-C data processing

We first trimmed the adapters of the Hi-C raw FASTQ files and then mapped the trimmed files against the hg19 human reference genome using the runHi-C pipeline, which is based on the 4DN consortium. Specifically, Burrows-Wheeler Aligner was used for the FASTQ file alignment and aligned reads with low quality, and PCR duplicates were filtered. Aligned reads were then paired on the basis of read pairs and filtered for fragments that contained ligations of at least two different restriction fragments. These reads were then binned at 5-kb resolution. To generate the contact matrix at multiple resolutions (5, 10, 25, 40, 50, 100, 250, 500 kb, 1, 2.5, 5, and 10 Mb), we used the run-cool2multirescool script from 4DN consortium, which performed the ICE normalization at the same time. We used Coolbox to visualize ICE-normalized genomic Hi-C data. The juicer tool was also used to generate multiresolution .hic files, which can be visualized using Juicebox.

RNA extraction

RNA was extracted using a Yeasen MolPure Cell RNA Kit. according to the manufacturer’s instructions. The resulting RNA was stored at -80℃ until further use.

RT-qPCR

Extracted RNA was quantified using a Nanodrop Spectrophotometer. 1μg RNA was used to generate cDNA using the HiScript III RT SuperMix for qPCR (Vazyme) according to the manufacturer’s instructions. Reactions were performed in technical duplicates using the ChamQ SYBR qPCR Master Mix (Vazyme) and indicated primer pairs on a machine (Applied Biosystems).

RT-qPCR primers

Name	**Sequence 5’-3’**
IL3-F	CGCGGATCCAAACATGAGCCGCCT
IL3-R	GCTCTAGATGCCGCAGGAAAAGGTGAA
IL5-F	ATGAGGATGCTTCTGCATTTG
IL5-R	TCAACTTTCTATTATCCACTCGGTGTTCATTAC
P4HA2-F	CAAACTGGTGAAGCGGCTAAA
P4HA2-R	GCACAGAGAGGTTGGCGATA
Actin-F	TATGAGCTGCCTGACGGC
Actin-R	CAGCAATGCCTGGGTACA

Statistics

The data presented in this study are expressed as the mean of at least three independent experiments ± SEM. Statistical analysis was carried out using GraphPad Prism 9 software, with unpaired two-sided Student’s t-tests, one-way analysis of variance (ANOVA) with Kruskal-Wallis test with Dunn’s multiple comparisons test, as appropriate. Survival analysis was performed using Gehan-Breslow-Wilcoxon test. Statistical significance was considered to be achieved when $p < 0.05$. All experiments were repeated a minimum of three times unless otherwise indicated.

Data availability

The raw sequencing data from this study have been deposited in the Genome Sequence Archive(6) in National Genomics Data Center(7), Beijing Institute of Genomics (BIG), Chinese Academy of Sciences, under the accession number: HRA004277, which is publicly accessible at https://ngdc.cncb.ac.cn/gsa.

We also host a UCSC browser session for easy access and viewing of genome-wide mapping at:

http://genome-asia.ucsc.edu/s/xuwenqian/RJ9_data

All other relevant data that support the conclusions of the study are available from the authors on request. Please contact jdh12262@rjh.com.cn.

Supplementary Figures

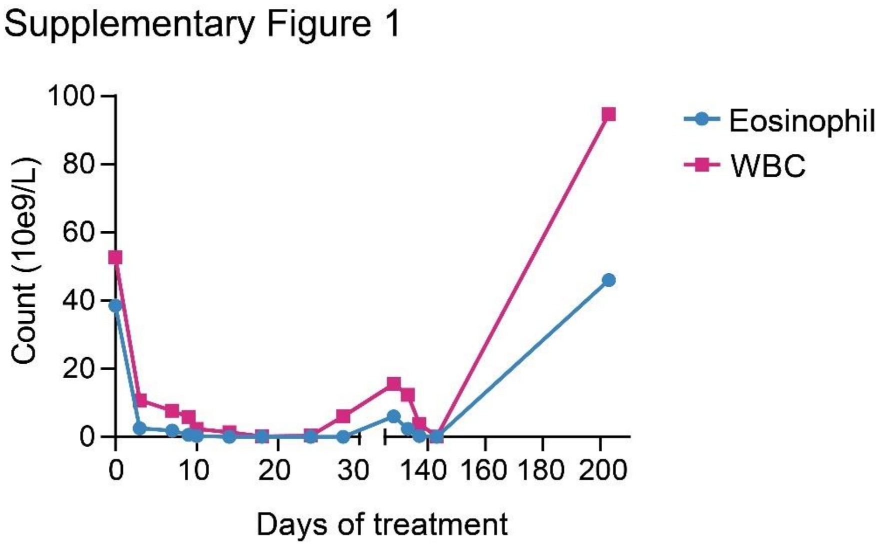

Supplementary Fig. S1 Correlation between eosinophils and leukocytes in the patient sample.

The *x* axis represents the treatment days of the *ETV6::ACSL6* ALL patient, and the *y* axis represents the cell count in the peripheral blood of the patient.

Supplementary Figure 2

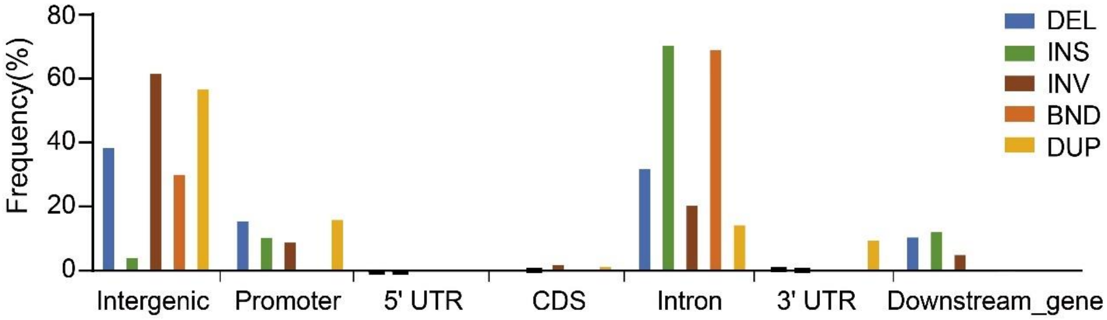

Supplementary Fig. S2 ONT detecting structural variations in *ETV6::ACSL6* ALL

Breakpoint enrichment from each SV type distributed in different genomic regions. DEL, deletion; INS, insertion; INV, inversion; BND, breakpoint end of translocation; DUP, duplication.

Supplementary Figure 3

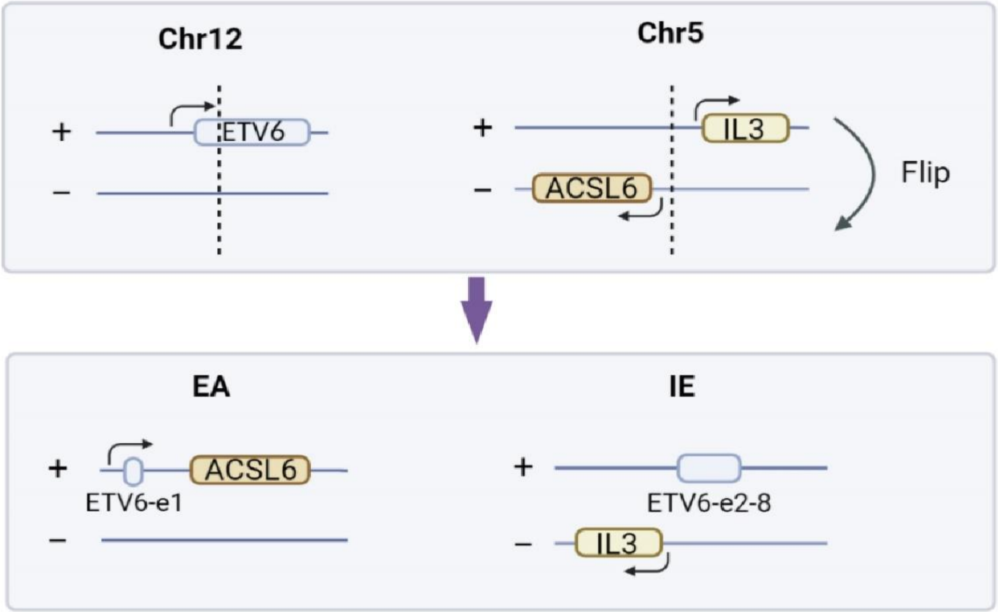

Supplementary Fig. S3 Graphical illustration of newly formed chromosomes

Blue square, *ETV6*, yellow square, *IL-3*, orange square, *ACSL6*. e, exon.

Supplementary Figure 4

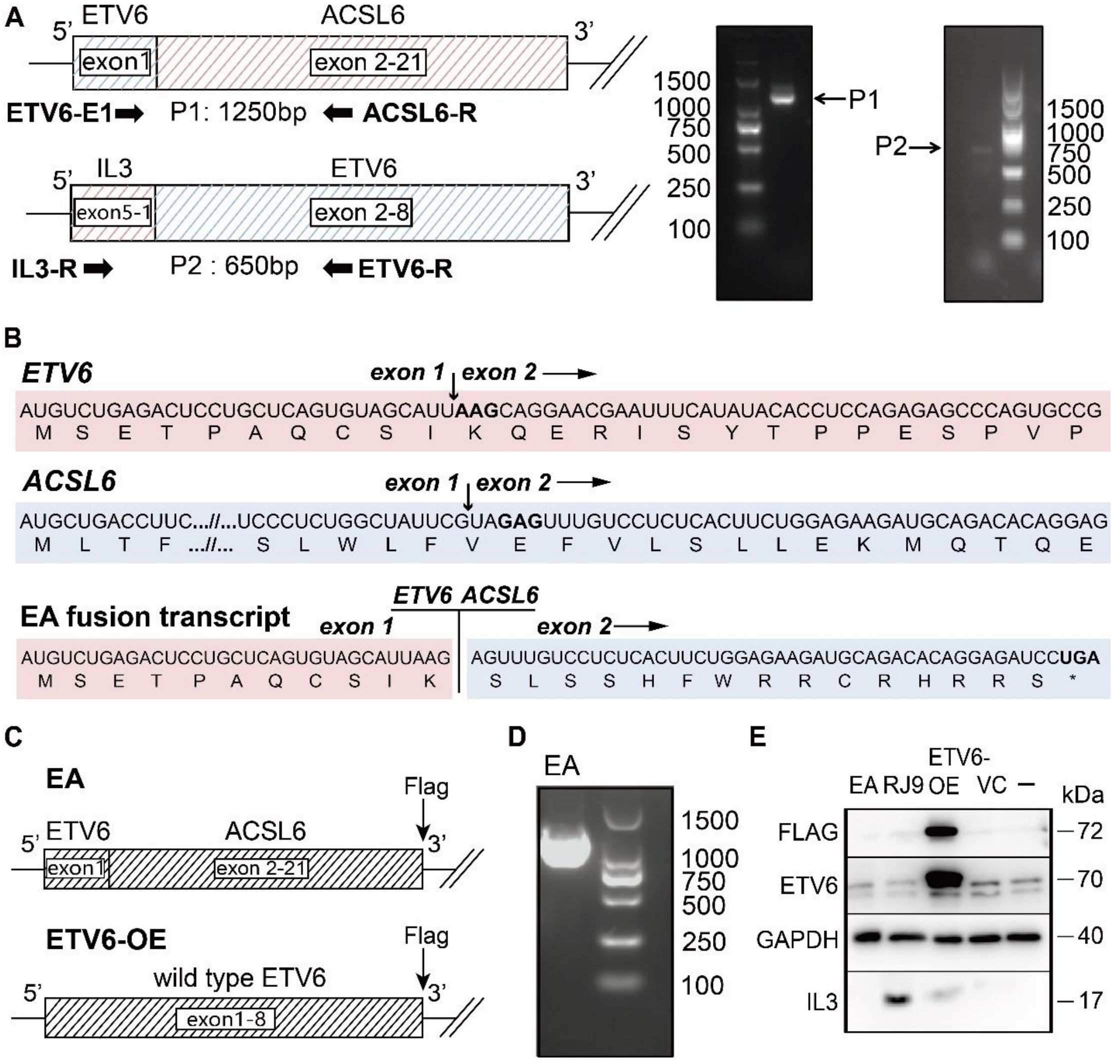

Supplementary Fig. S4 Deciphering *ETV6::ACSL6* at the RNA level

(A) Schematic diagram of the fusion of two chromosomes at the cDNA level. Primers are shown in black arrows. Right, electropherogram of PCR products. (B) mRNA of *ETV6*, *ACSL6* and the fusion gene. In each box, the upper part represents the codon sequence, and the lower part represents the corresponding amino acids. Breakpoints at the mRNA level are indicated by vertical arrows. On *ETV6* and *ACSL6*, codons near the breakpoints are highlighted in bold. The premature stop codon is indicated in bold, and an asterisk represents transcription termination. (C) A schematic diagram of the overexpression vector in Nalm6. Upper part, 3×Flag is inserted upstream of the 3' UTR of the fusion gene; Lower part, overexpression of wild-type *ETV6*, with 3×Flag inserted at 3' end. OE, overexpression. (D) Electropherogram of PCR products validating expression of *ETV6::ACSL6* transcript. (E) Western blot analysis of IL3, Flag and ETV6 protein levels of RJ-9 PDX cells and Nalm6 after transfection. ETV6-OE, overexpression of wild-type *ETV6* with 3×Flag; VC, vehicle control; -, non-transfected Nalm6 cells.

Supplementary Figure 5

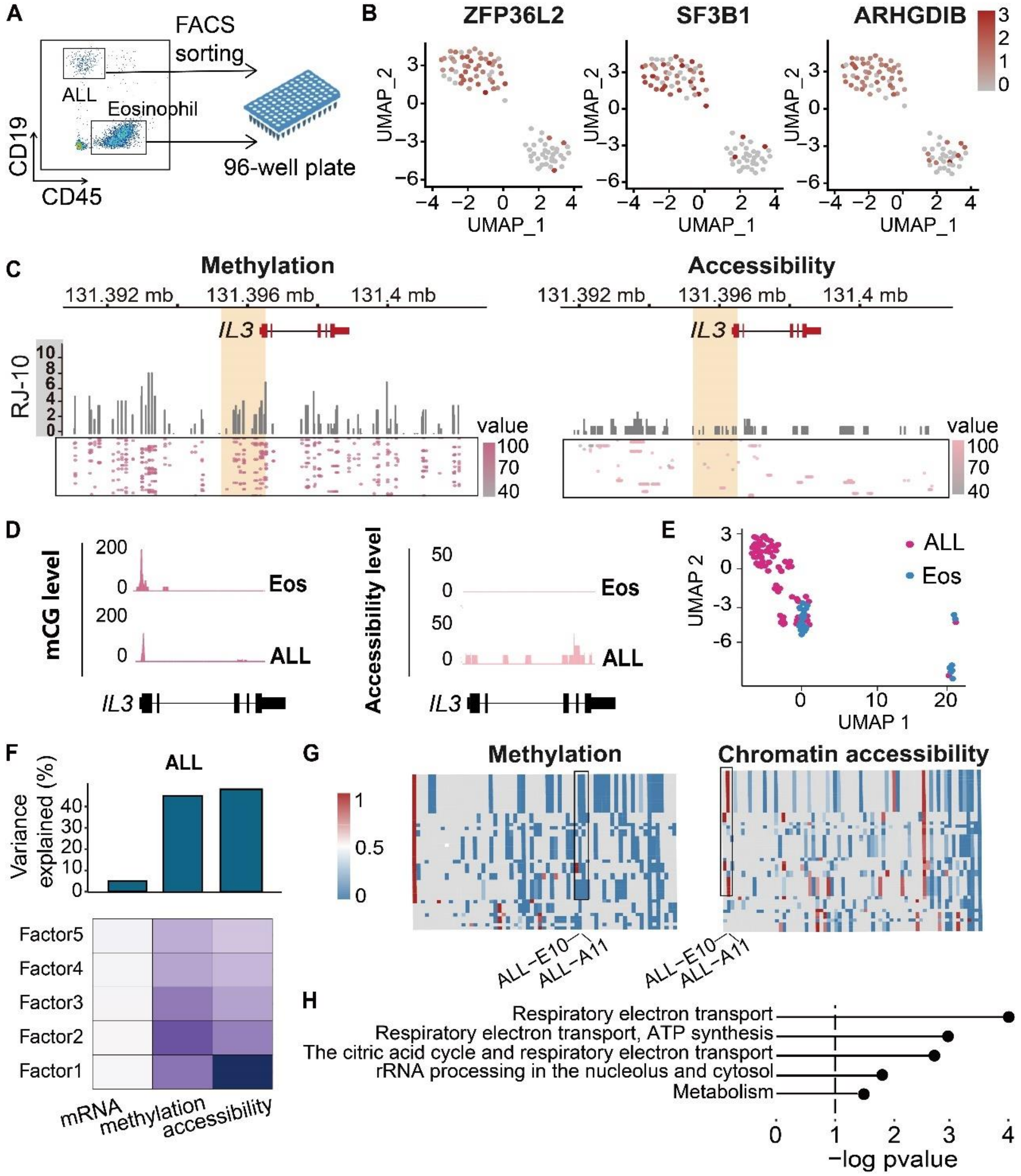

Supplementary Fig. S5 Single-cell sequencing dissecting heterogeneity within ALL cells.

(A) Single cells of blasts and eosinophils were sorted using FACS into 96-well plates. Cells shown were gated on live singlets. (B) UMAP dimensionality reduction displaying scRNA data of indicating genes. (C) Left, single-cell methylation data at IL-3 loci. Right, single-cell accessibility data at IL-3 loci. Bar plot showing the average level of all cells detected at indicated genomic loci. Each row in the box corresponds to a single cell. Each dot represents the methylation or accessibility level of the corresponding cell (horizontally) at the corresponding genomic position (vertically). RJ-10, a normal karyotype ALL patient. (D) Left, coverage tracks of single-cell methylation (mCpG) data at the IL-3 locus. Right, coverage tracks of single-cell accessibility data (GpCm) at the IL-3 locus. (E) UMAP projection based on the MOFA factors that integrated RNA-seq, mCpG and GpCm datasets from ALLs and eosinophils (n=89). Cells are colored based on cell types. Pink dots, ALL cells; Blue dots, eosinophils. (F) Percentage of variance explained (R^2) by each MOFA factor (bottom rows) across all three layers. Top bar plot, the sum of all factors as a proportion. (G) Heatmap of methylation data in MOFA factor2 and chromatin accessibility data in MOFA factor1. Gray box, data not available. (H) GSEA analysis of characteristic genes of MOFA factor1 and MOFA factor2, overlapping pathway of two MOFA factors are shown.

Supplementary Figure 6

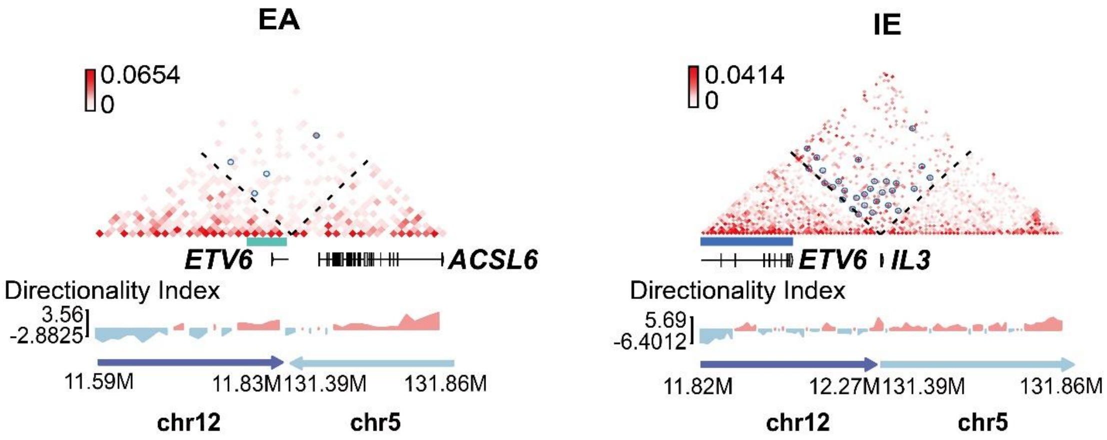

Supplementary Fig. S6 Neo-TADs in *ETV6::ACSL6* ALL cells

Reconstructed Hi-C map indicating two neo-TADs following translocation. Neo-loops are showed in blue circles.

Supplementary Figure 7

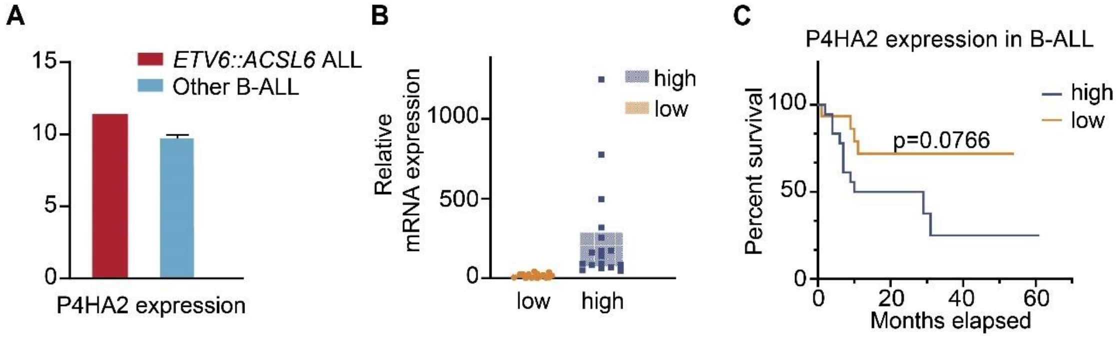

Supplementary Fig. S7 P4HA2 expression level and outcome of ALL patients.

(A) Expression analysis of *P4HA2* in *ETV6::ACSL6* ALL as compared with other 31 B-ALL patients. Gene expression was quantified by RNA-seq (log2 of counts normalized using DESeq2’s median of ratios). (B) RT-qPCR validation of *P4HA2* expression in different ALL cases. Comparison analysis was performed by the Wilcoxon rank-sum test. (C) Kaplan-Meier curves for B-ALL patients grouped by *P4HA2* expression.

Supplementary Figure 8

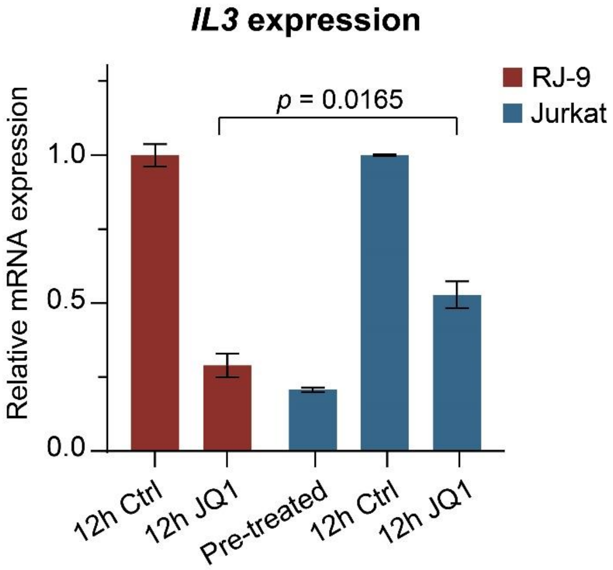

Supplementary Fig. S8 BRD4 inhibitors demonstrated a mild impact on *IL3* expression in Jurkat cells

IL3 expression of RJ-9 PDX cells and Jurkat cell line treated with 1 μM JQ1 for 12h. RJ-9, *ETV6::ACSL6* ALL. Before JQ1, Jurkat was pre-stimulated with both PHA (2 μg/ml) and PMA (20 ng/ml) for 4 hours. 12h Ctrl and 12h JQ1 in blue, Jurkat cells treated by vehicle (0.02% DMSO) or JQ1 (1 μM) for 12 hours following the stimulation of *IL3* expression. A total of n = 3 independent experiments are plotted as mean ± SEM.

Supplementary Figure 9

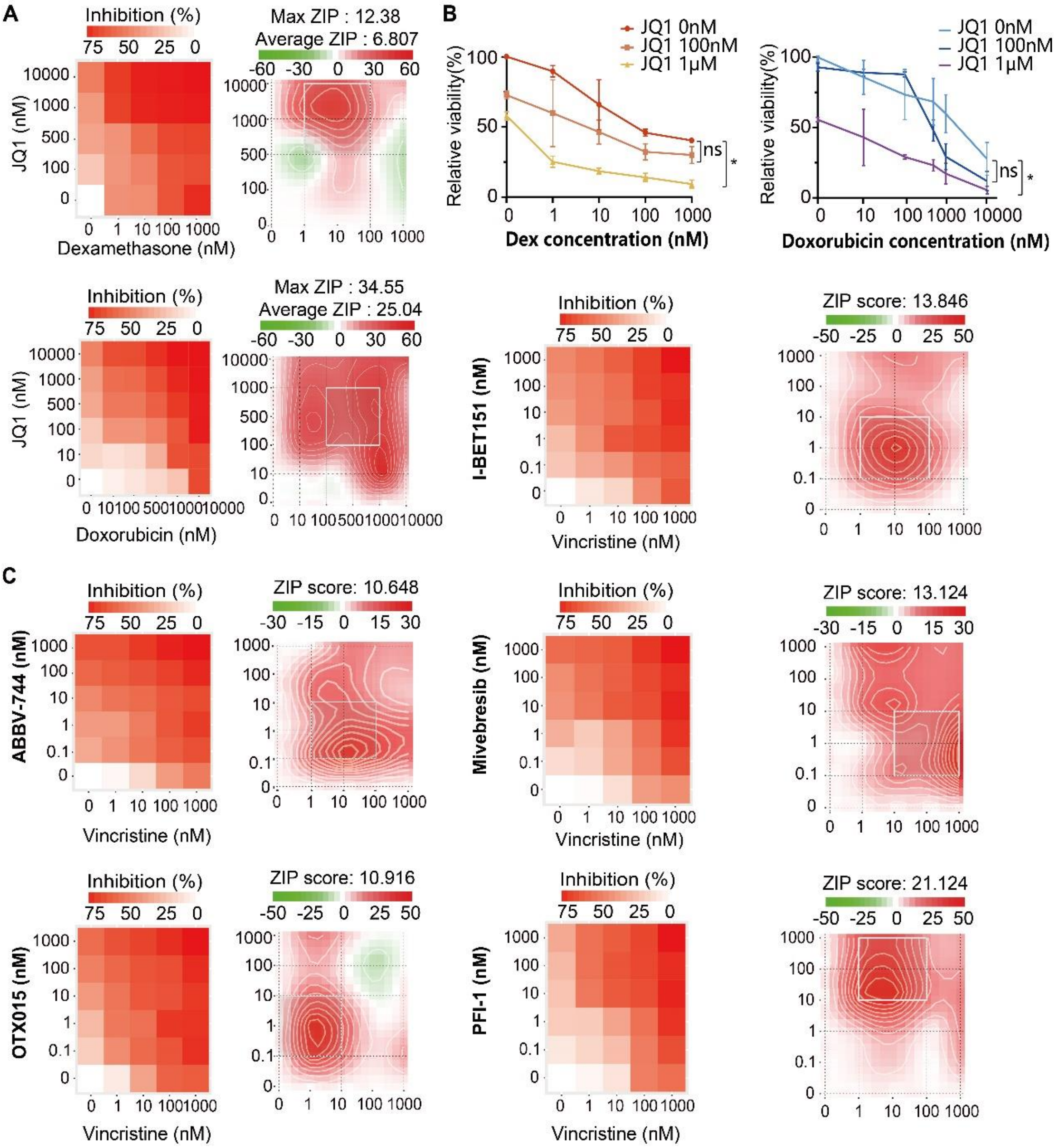

Supplementary Fig. S9 ALL cells exhibited vulnerability to BRD4 inhibitors.

(A) Cytotoxicity assay determined the synergy of JQ1 and dexamethasone/doxorubicin in inducing cell death of RJ-9 cells. ZIP, ZIP synergy score. (B) Cytotoxic assay of JQ1 and dexamethasone/doxorubicin at indicating concentrations. *$p < 0.05$. (C) ZIP score of vincristine with indicating BRD4 inhibitors through *in vitro* cytotoxicity assay.

Supplementary Figure 10

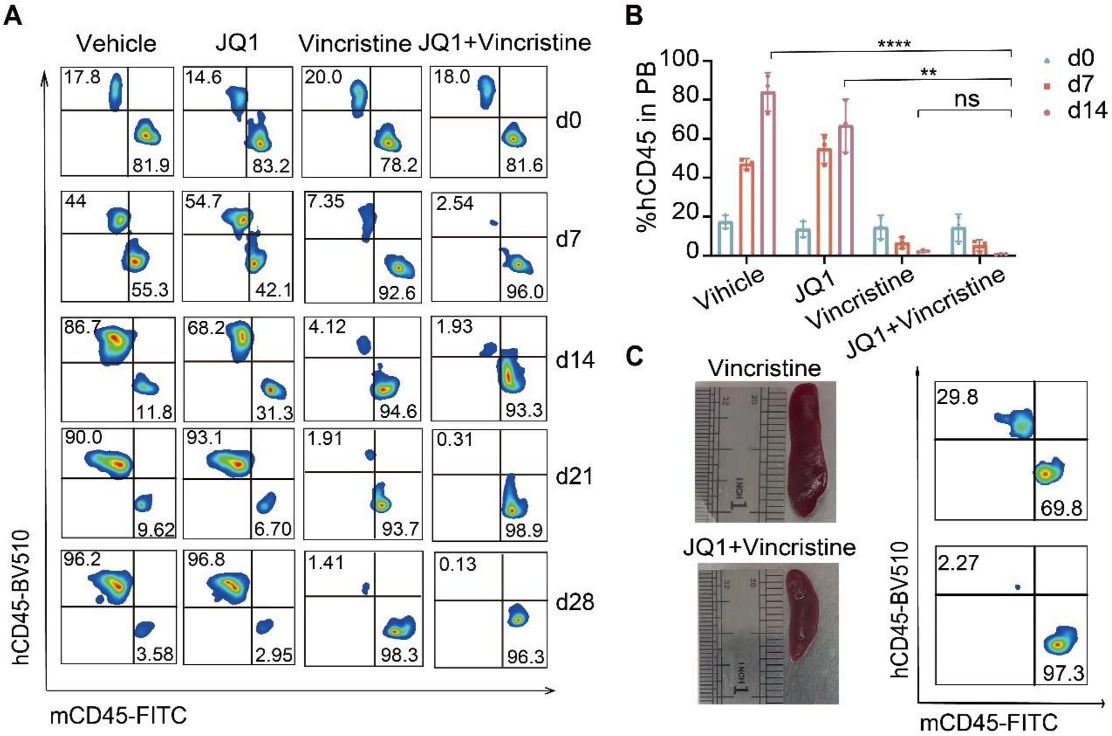

Supplementary Fig. S10 BRD4 inhibitors demonstrated anti-tumor effects *in vivo* on ALL cells.

(A) Flowcytometry of leukemia cells in the peripheral blood on indicated days of treatment. (B) Proportion of leukemia cells in peripheral blood on indicated days of treatment. n.s., not significant, **p < 0.01, ****p < 0.0001. (C) Tumor burden in the spleens of VCR alone (top) and VCR+JQ1 (bottom) at day 28 of treatment. Flow cytometry data of the corresponding leukemia cells in the spleen are on the right.

Supplementary References

1. Jing D, Bhadri VA, Beck D, Thoms JA, Yakob NA, Wong JW, Knezevic K, Pimanda JE, Lock RB. Opposing regulation of BIM and BCL2 controls glucocorticoid-induced apoptosis of pediatric acute lymphoblastic leukemia cells. Blood. 2015; 125(2):273-83.

2. Yu CH, Wu G, Chang CC, Jou ST, Lu MY, Lin KH, Chen SH, Wu KH, Huang FL, Cheng CN, Chang HH, Hedges D, Wang JL, Yen HJ, Li MJ, Chou SW, Hung CT, Lin ZS, Lin CY, Chen HY, Ni YL, Hsu YC, Lin DT, Lin SW, Yang JJ, Pui CH, Yu SL, Yang YL. Sequential Approach to Improve the Molecular Classification of Childhood Acute Lymphoblastic Leukemia. J Mol Diagn. 2022; 24(11):1195-1206.

3. Gao M, Wang J, Rousseaux S, Tan M, Pan L, Peng L, Wang S, Xu W, Ren J, Liu Y, Spinck M, Barral S, Wang T, Chuffart F, Bourova-Flin E, Puthier D, Curtet S, Bargier L, Cheng Z, Neumann H, Li J, Zhao Y, Mi JQ, Khochbin S. Metabolically controlled histone H4K5 acylation/acetylation ratio drives BRD4 genomic distribution. Cell Rep. 2021; 36(4):109460.

4. Belaghzal H, Dekker J, Gibcus JH. Hi-C 2.0: An optimized Hi-C procedure for high-resolution genome-wide mapping of chromosome conformation. Methods. 2017; 123:56-65.

5. Kaya-Okur HS, Wu SJ, Codomo CA, Pledger ES, Bryson TD, Henikoff JG, Ahmad K, Henikoff S. CUT&Tag for efficient epigenomic profiling of small samples and single cells. Nat Commun. 2019; 10(1):1930.

6. Chen T, Chen X, Zhang S, Zhu J, Tang B, Wang A, Dong L, Zhang Z, Yu C, Sun Y, Chi L, Chen H, Zhai S, Sun Y, Lan L, Zhang X, Xiao J, Bao Y, Wang Y, Zhang Z, Zhao W. The Genome Sequence Archive Family: Toward Explosive Data Growth and Diverse Data Types. Genomics Proteomics Bioinformatics. 2021.

7. Database Resources of the National Genomics Data Center, China National Center for Bioinformation in 2022. Nucleic Acids Res. 2022; 50(D1):D27-d38.